New insights on atrial fibrillation mechanisms through the analysis of structural and electrical features

Presentata da: **Maddalena Valinoti**

For all those who have always believed in me.

A chi ha sempre creduto in me.

Abbreviations

AA: atrial activation

AF: atrial fibrillation

AS: analytic signal

CT: computed tomography

DF: dominant frequency

EAM: electroanatomic mapping

ECG: electrocardiogram

EGM: electrogram

FIRM: focal impulse and rotor modulation

HT: Hilbert transform

LA: left atrium

LAAT: local atrial activation timing

LGE-MRI: late-gadolinium enhancement

MRA: magnetic resonance angiography

MRI: magnetic resonance imaging

NDSR: negative derivative sinusoidal recomposition

PS: phase singularity

PV: pulmonary veins

RFCA: radiofrequency catheter ablation

SEGM: synthetic electrogram

SR: sinusoidal recomposition

TE: echo-time

TR: recovery time

VA: ventricular activation

Abstract

Atrial fibrillation is the most common type of arrhythmia encountered in clinical practice but its maintaining mechanisms remain elusive. Radiofrequency catheter ablation is a non-pharmacological therapy that aims to restore sinus rhythm ablating tissue that facilitates atrial fibrillation perpetuation and is more effective than medications. Neverthless, rigorous monitoring after the ablation procedures showed atrial fibrillation recurrence in about 40% to 60% of cases for one procedure and in about 70% of cases for three or more procedures.

Over the last years, theories based on the structural and electrical remodeling have been proposed to target atrial fibrillation mechanisms.

It is well known that the hallmarks of the structural changes during atrial fibrillation are the fibrosis tissue generation and left atrium dilatation. According to recent studies, the success rate of the ablation procedure and the induction of atrial fibrillation depends on the atrial fibrotic tissue extent on the atrial wall. Other studies ascribe the ablation failure to left atrium enlargement occurring during the arrhythmia.

One of the theories on atrial electrical remodeling in atrial fibrillation, strongly debated in the Electrophysiology Community, is the "Rotor Theory". Recently, a study guided by a proprietary navigation system, showed the presence of stable electrical rotors whose ablation may improve the outocome of the ablation procedure. Other studies did not confirm these results.

The aim of this thesis is to provide computational approaches to better investi-

gate the existence of the electrical rotors and the role of the left atrium structural alterations as potential primary mechanisms sustaining atrial fibrillation.

The thesis is composed by four chapters. The first chapter introduces the atrial fibrillation and describes in details the electrical rotor and the structural remodeling phenomena identified as possible maintaining mechanisms for atrial fibrillation.

The second chapter regards the structural characterization of the left atrium through the development of a fully-automated approach for 3D left atrium fibrosis patient specific model construction and left atrium volume estimation. In this chapter are presented several imaging techniques that were applied on magnetic resonance imaging data. In particular, in oder to obtain the 3D left atrium patient-specific model, a new fully-automated approach for the left atrium segmentation on magnetic resonance angiography is described and a multimodality affine registration, used to superimpose the fibrosis information derived from the late-gadolinium enhancement on the 3D model, is presented. In addition several techinques for the fibrosis quantification are showed in details. Furthermore, for the left atrium volume estimation, an approach able to remove the pulmonary veins from the 3D left atrium model is designed and the qualitative and quantitative results on fibrosis extent and left atrium volume computation are showed. The third chapter regards the electrical characterization of the left atrium throught the development of an independent approach for the rotor localization on 3D left atrium surface based on the phase analysis of the unipolar electrograms. In particular a new version of the sinusoidal recomposition method for local atrial activation detection and for phase map construction is described and a rotor detection algorithm based on the phase singularity concept is described. The chapter also exhibits the development of a synthetic electrogram generator, used for testing of the local atrial activation detection, and the validation of the rotor localization using an atrial computational model. The results of the validations are illustrated in details and in addition the results on clinical data are presented. Furthermore, this chapter shows the analysis conducted and its results on the influence of the spatial coverage of the catheter on rotor localiza-

tion.

Finally in the fourth chapter some conclusive remarks are presented with possible future developments of the presented work.

Overall this PhD project wants to provide a better understanding the mechanisms promoting the initiation, progression and maintenance of atrial fibrillation through the development of imaging and signal processing computational approaches.

Abstract

Il progetto di Dottorato presentato si colloca nell'ambito della fibrillazione atriale, la quale risulta essere una delle aritmie maggiormente riscontrate nella pratica clinica. Nel corso degli ultimi anni si sono sviluppate metodiche che hanno consentito di trattare la fibrillazione atriale mediante ablazione transcatetere con radiofrequenza, terapia che si è dimostrata molto efficace nel ripristino del ritmo sinusale, eliminando il tessuto responsabile dell'aritmia stessa. Nonostante l'ablazione sia una delle terapia più promettenti per la fibrillazione atriale, la percentuale di successo dopo una singola procedura di ablazione resta del 40%-60%, circa del 70% dopo tre o più procedure. Tali percentuali suggeriscono che i meccanismi che regolano e sostengono la fibrillazione atriale non sono ancora ben compresi e pertanto una strategia ablativa ottimale non è ancora disponibile. A tal proposito si sono sviluppate diverse teorie sui meccanismi alla base della fibrillazione atriale basate sul rimodellamento strutturale ed elettrico dell'atrio sinistro.

È risaputo che i cambiamenti strutturali dell'atrio sinistro durante l'aritmia sono attribuibili alla generazione del tessuto fibrotico sulla parete atriale e alla dilatazione dell'atrio sinistro. Secondo studi recenti, il tasso di successo delle procedure di ablazione, così come la generazione della fibrillazione atriale, dipendono dalla percentuale di tessuto fibrotico sulla parete; altri studi adducono il fallimento dell'ablazione ad un aumento delle dimensioni dell'atrio sinistro, causato dall'aritmia stessa.

Una delle teorie sul rimodellamento elettrico dell'atrio, fortemente discussa nella comunità scientifica di elettrofisiologia, è la "teoria dei rotori". Uno studio molto recente, ha dimostrato la presenza di "rotori" o "onde a spirali" stabili nello spazio, la cui ablazione incrementa notevolmente la percentuale di successo della procedura. Studi successivi condotti da altri gruppi di ricerca, non hanno confermato la presenza di rotori.

Lo scopo di questo lavoro di tesi è quello di investigare il ruolo dei rotori elettrici e delle alterazioni strutturali dell'atrio sinistro come potenziali meccanismi responsabili della generazione e del sostentamento della fibrillazione atriale.

La tesi è strutturata in quattro capitoli. Il primo capitolo introduce la fibrillazione atriale e descrive nel dettaglio i rotori elettrici e i fenomeni alla base del rimodellamento strutturale, identificati come possibili responsabili del sostentamento della fibrillazione atriale.

Il secondo capitolo riguarda la caratterizzazione strutturale dell'atrio sinistro attraverso lo sviluppo di un metodo completamente automatico atto alla costruzione di un modello 3D paziente-specifico della fibrosi dell'atrio sinistro e alla stima della volumetria atriale. In questo capitolo vengono presentate le diverse tecniche di imaging, applicate su dati di risonanza magnetica e utilizzate per la generazione del modello 3D. In particolare, viene descritto un nuovo metodo completamente automatico per la segmentazione dell'atrio sinistro a partire da immagini di risonanza magnetica angiografica ed è stato utilizzato un metodo di registrazione affine multimodale per sovrapporre l'informazione sulla fibrosi ottenuta dai dati di risonanza magnetica con il late gadolinium enhancement sul modello 3D ricostruito. Inoltre nel capitolo sono mostrate diverse tecniche di quantificazione della fibrosi e viene presentato anche un nuovo approccio per la rimozione delle vene polmonari dal modello 3D dell'atrio. Infine vengono presentati i risultati qualitativi e quantitativi della volumetria atriale stimata e della distribuzione del tessuto fibrotico sulla parete atriale.

Il terzo capitolo riguarda la caratterizzazione elettrica dell'atrio sinistro attraverso lo sviluppo di un approccio indipendente per la localizzazione dei rotori sulla superficie 3D dell'atrio sinistro, basato sull'analisi in fase degli elet-

trogrammi unipolari. In particolare, viene presentata una nuova versione del metodo di ricomposizione sinusoidale, per una migliore detezione degli istanti di attivazione atriale e per una ricostruzione 3D della mappe di fase più accurata.

La seconda parte del capitolo si focalizza sulla descrizione dell'algoritmo di detezione dei rotori basato sul concetto di singolarità di fase. Inoltre viene presentato lo sviluppo di un generatore di elettrogrammi sintetici, usato per testare la detezione degli istanti di attivazione atriale, e la validazione della localizzazione dei rotori attraverso l'utilizzo di un modello computazionale dell'atrio sinistro. Vengono presentati nel dettaglio i risultati delle validazioni ed i risultati ottenuti sui dati clinici. Inoltre questo capitolo mostra l'analisi condotta e i risultati ottenuti sull'importanza della copertura spaziale del catetere nella localizzazione dei rotori.

Nel quarto capitolo sono presentate delle osservazioni conclusive e possibili sviluppi futuri del presente lavoro.

In generale questo progetto di dottorato ambisce a fornire una migliore comprensione dei meccanismi relativi all'innescamento, alla progressione e alla persistenza della fibrillazione atriale attraverso lo sviluppo di nuovi metodi basati sull'elaborazione di immagini di risonanza magnetica e di segnali intracavitari.

Contents

13

14

Chapter 1

Introduction

AF is the most common type of cardiac arrhythmia characterized by an irregular and rapid beating of the atria.

Despite big efforts to improve AF efficacy, its therapies remain suboptimal because the maintaining mechanisms of AF are not clearly identified. In this regards, over the last years, various theories were proposed to improve the outcome of AF treatments.

1.1 AF: epidemiology and clinical implications

AF is the leading cause of hospitalization and death [1]. Despite good progress in the management of patients affected by AF, this arrhythmia remains one of the major causes of stroke, heart failure, sudden death and cardiovascular morbidity in the world [2].

In 2010, the estimated number of the individuals with AF worldwide was 33.5 million (20.9 million males and 12.6 million females), with the higher incidence in developed countries [3, 4]. The Cardiovascular Heart Study showed that the age-specific prevalence is higher in men than women and this difference becomes

equal in older age. The prevalences in the age group 65– 69 years were 5.8% and 2.8% in men and women, respectively; and in the age group 70 –79 years, the prevalence was almost equal in men and women: 5.9% and 5.8%, respectively, due to the longer life expectancy in women [5, 6]. In Europe over 4.5 million of people are affected by AF and in 2030 the expected number will be 14-17 million with the number of new cases of AF per year of 120.000 - 215.000 [4, 7, 8]. In US people affected by AF are 3 millions [9]. The prevalence of AF increases with the age. It is 1% in the general population and increases from 0.1% among adults younger than 55 years to 9% among octogenerians. Approximately 70% of individuals with AF are between 65 and 85 years of age. Apart from advancing age, other risk factors for AF are: hypertension, diabetes mellitus, valvular heart disease and congestive heart failure [5, 10]. Hospitalization is the primary cost driver in the management of AF and the economic burden is nontrivial [11]. Some studies have identified annual costs for AF in 2005 of 6.65 million dollars in US and 459 million pounds in UK [12, 13]. These costs with the increasing prevalence justify increased attention to the management of patients with AF. In AF, heart electrical signals do not begin in the sinoatrial node, but in other part of the atria, especially near the ostia of the PVs. The signals spread throughout the atria in a rapid and disorganized way, causing their fibrillation. Patients with AF, may have no symptoms (asymptomatic AF) or suffer of a variety of symptoms including: palpitations or a fluttering heartbeat, irregular heartbeat, chest pains, dizziness and fainting spells (Figure 1.1) .

Chaotic electrical activation in the atria associated with AF, manifests in the ECG as undistinguishable P waves due to the asynchronous depolarization of atrial tissue. Atrial rates detected from the ECG in AF vary between 400-600 "beats" per minute (bpm). In some cases the pattern of atrial activity can be similar to atrial flutter, mostly regular and with high amplitude, or both. During AF, the RR intervals is commonly irregular, varing in a range 110-180 bpm [14]. Fortunately, the atrioventricular node does not allow many signals through to the ventricles; about 1 or 2 out of every 3 atrial activations passes to the ventricles (Figure 1.2). According to AF duration, success of cardioversion

16
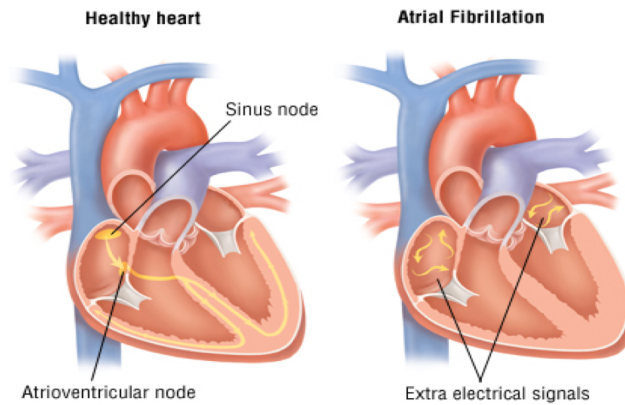
Figure 1.1: Electrical pathway in sinus condition (left) and in atrial fibrillation (right).
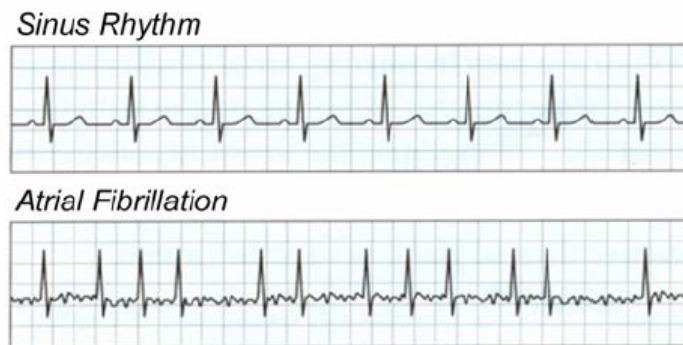
Figure 1.2: ECG signals in sinus rhythm (top) and AF condition (bottom).

techniques and capacity of restarting, five different types of AF are traditionally distinguished [2, 15, 16]:

- First diagnosed: AF that has not been diagnosed before, irrespective of the duration of the arrhythmia or the presence and severity of AF-related symptoms.

- Paroxysmal AF: self-terminating in most cases within 48 hours. Some AF paroxysms may continue for up to 7 days. AF episodes that are cardioverted within 7 days should be considered paroxysmal.

17

- Persistent AF: AF that lasts longer than 7 days, including episodes that are terminated by cardioversion, either with drugs or by direct current cardioversion, after 7 days or more.

- Long-standing persistent AF: continous AF lasting for ≥ 1 year when it is decided to adopt a pharmacological rhythm control strategy.

- Permanent AF: AF that is accepted by the patient (and physician). Hence, rhythm control interventions are, by definition, not pursued in patients with permanent AF. Should a rhythm control strategy be adopted, the arrhythmia would be re-classified as 'long-standing persistent AF'.

The therapies for AF management consist of pharmacological and non-pharmacological treatments. Antiarrhythmic drugs can be used for rate control of chronic atrial fibrillation, cardioversion of atrial fibrillation to sinus rhythm, maintenance of sinus rhythm after the cardioversion. Antiarrhythmic drugs comprise many different drug classes and have several different mechanisms of action. Furthermore, some classes and even some specific drugs within a class

Class	Examples	Mechanism
Ia	Quinidine Procainamide	Na⁺ channel blockers (intermediate association/dissociation)
Ib	Lidocaine Phenytoin	Na⁺ channel blockers (fast association/dissociation)
Ic	Flecainide Propafenone	Na⁺ channel blockers (slow association/dissociation)
II	Propranolol Metoprolol	Beta blockers (propanolol also shows some class I action)
III	Amiodarone Sotalol	K⁺ channel blockers (sotalol is also a beta blocker; amiodarone has Class I, II, III, and IV activity)
IV	Verapamil Diltiazem	Ca²⁺ channel blockers
V	Adenosine Digoxin	Work by unknown mechanisms (direct nodal inhibition)

Figure 1.3: Vaughan-Williams classification

are effective with only certain types of arrhythmias. The first scheme that was proposed for drug administration, the Vaughan-Williams classification, is still the most used in clinical practice. [17], (Figure 1.3). Antiarrhythmic drug

action is usually insufficient by itself and it often requires application of the non-pharmacological therapies in order to restore the sinus rhythm. Reasons for choosing non-pharmacological therapy may be paroxysmal atrial fibrillation with very frequent attacks and severe symptoms, chronic atrial fibrillation without adequate rate control, leaving the patient at risk of developing tachycardiomyopathy, or patients who experience intolerable side effects of otherwise effective drug therapy [18]. Non - pharmacological treatments include electrical shock therapy (also known as defibrillation or cardioversion), implanting a short-term heart pacemaker or RFCA.

1.2 RFCA

Catheter ablation of AF is a non-pharmacological therapy more effective than medications. It consists in of an invasive procedure that aims to restore the sinus rhythm by eliminating tissue causing AF with radiofrequency energy. The procedure is carried out in the Electrophysiology lab using fluoroscopy and a 3D EAM system. The 3D navigation system combines anatomic and electrical information by a catheter point-by-point mapping, allowing a 3D anatomic reconstruction of a 3D shell of the targeted cardiac chamber (Figure 1.4a). There are two different EAM systems that are widely used in clinical practice. The CARTO mapping system (Biosense Webster Inc., NJ, USA) relies on both a magnet-based localization for visualization of the ablation catheter and an impedence-based system that allows for both tip and catheter curve visualization as well as simultaneous visualization of multiple electrodes. The second one is an electrical impedence mapping system (NavX, St. Jude Medical Inc., MN, USA) using voltage and impedence for localization. Recently, a third EAM avaible in clinical practice is the magnetic and electrical Rhythmia mapping system (Boston Scientific, MA, USA), which is an EAM system that allows for automated high density mapping using a dedicated 64-electrodes mini basket catheter [19].

The use of these 3D mapping systems has been demonstrated to reduce fluoroscopy duration [20, 21].

To improve the anatomical accuracy of the map, integration of 3D images obtained by CT or MRI has become available. Despite CT and MRI are not real-time images and their registration with the navigation system spatial domain might be not accurate, some studies sustain that the use of EAM system with the image integration improves the safety and the efficacy of the ablation procedure [22, 23, 24].

More than 15 years ago, Haissaguerre et al. [25] revealed ectopic beats from the PVs may trigger AF, establishing the field of AF ablation with PV isolation as its cornerstone. The ablation consists of a series of point -by-point radiofrequency lesions encircling the ostia of the PVs using the ablation catheter inserted through the femoral vein (Figure 1.4b), [26]. Cryoablation is another technique
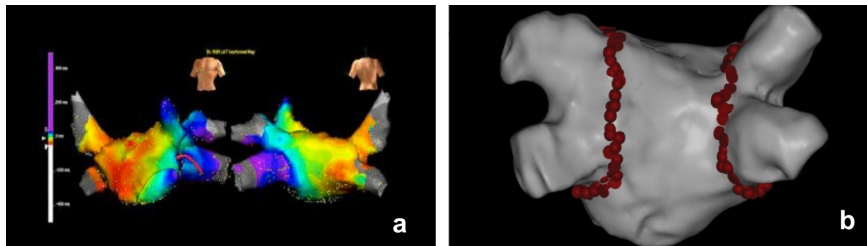
Figure 1.4: a) Electroanatomical map; b) 3D reconstruction of the LA with circumferential ablation lesions (red points) arround the ostia pf the PVs

developed as a tool for AF ablation. Cryoablation systems work by delivering liquid nitrous oxide under pressure through the catheter to its tip or within the balloon, where it changes to gas, resulting in cooling of surrounding tissue. This gas is then carried back through the reciprocating vacuum lumen. The mechanism of tissue injury results from tissue freezing with a creation of ice crystals within the cell that disrupts cell membranes and interrupts both cellular metabolism and any electrical activity in that cell [27]. A study conducted in 2016 [28] reported no differences in efficacy and patient safety between the two kind of ablations.

Electrical isolation of the PVs is recommended during all AF ablation procedures. Despite the importance of this ablation endpoints, AF recurrence rate, observed especially in patients with persistent AF, remains high. PV isolation conveys a 60-80% rate of maintaining sinus rhythm after 1 year in patients with paroxysmal form of AF and about 50-60%in patients with persistent AF [29]. A study published by Ganesan et al. [30] demonstrated that the single procedure success for paroxysmal AF was 68.6% at 1 year, 61.1% at 3 years and 62.3% at 5 years. Comparing patients with persistent and long-standing persistent AF after a single procedure the results were less favorable, 50.8% at 1 year, and 41.6% at 3 years. This percentages suggest the maintaining mechanisms of AF are still unclear or partially known especially for the persistent AF. In this regards, recently, new insights on structural and electrical remodeling of LA during AF and additive strategies to the PV isolation were proposed to target AF mechanisms.

1.3   LA remodeling in AF

AF results from continuous remodeling of the LA, which involves electrical and structural remodeling transformations. These transformations are associated with the arrhythmia but they are also associated with the age and genetic factors. Electrical remodeling primarly reduces the refractory period and the action potential duration of the atria, while the structural remodeling impedes propagation and decreases the conduction velocity [31], promoting cell death, fibroblast proliferation and excess extracellular matrix production leading to fibrosis. Fibrotic lesions, preventing the electrical propagation, may favor the generation of reentry, as well as fibroblast-cardiomyocyte interactions promote reentry and ectopic impulse generation. On the other hand, AF itself may promote the structural alterations, creating a loop that contributes to the AF sustenance [32]. However, whether or not structural abnormalities observed in the atria are cause or consequence of AF, remains an open question. Another

aspect is the atrial enlargement that is probably associated with fibrosis generation. Atrial size was shown to be an important risk factor for AF recurrence [33] after the ablation and with the fibrotic tissue represents the core processes involved in structural remodeling.

1.3.1 Structural remodeling

Structural remodeling of the LA is characterized by fibrotic tissue generation and atrial enlargement. Fibroblasts represent an integral part of functioning myocardium by providing a cellular scaffold, maintaining a proper three-dimensional network required for normal mechanical function and contributing to the uniformity of the excitable substrate and to the uninterrupted and rapid propagation of electrical activation through the myocardium [34]. In addition to that, fibroblasts play an important role in the regulation of cardiomyocyte function by slowing down conduction in response to mechanical stretch [35], and in pathological conditions associated with AF, fibroblasts may proliferate, differentiate to myofibroblasts and increase production of extracellular matrix [36]. As a result of fibrosis development, the architecture of fibrotic myocardial tissue becomes heterogeneous, thereby affecting intercellular conduction [37] increasing its anisotropy and leading to conduction slowing, development of functional and structural block, thus creating the arrhythmic substrate [38].

Chronic animal models provide the opportunity to study the relationship between the fibrotic tissue and AF. A study conducted using a rapid atrial pacing (RAP)-induced chornic AF in dogs, demonstrated that the fibrosis increases both in the atrium and in the ventricle. The percentage of fibrosis in a control dog was about 2.0%, 10.1% after six months of AF dogs. The study also observed the presence of the fibrosis in the LV : 1.0% in a control dog, 2.4% after six months (Figure 1.5) [39].

LGE-MRI is a recent technique used for LA fibrosis distribution assessment on the atrial wall. LGE-MRI is capable of visualizing micro-fibrosis that cannot be detected by other imaging techniques and is performed about 15 minutes after
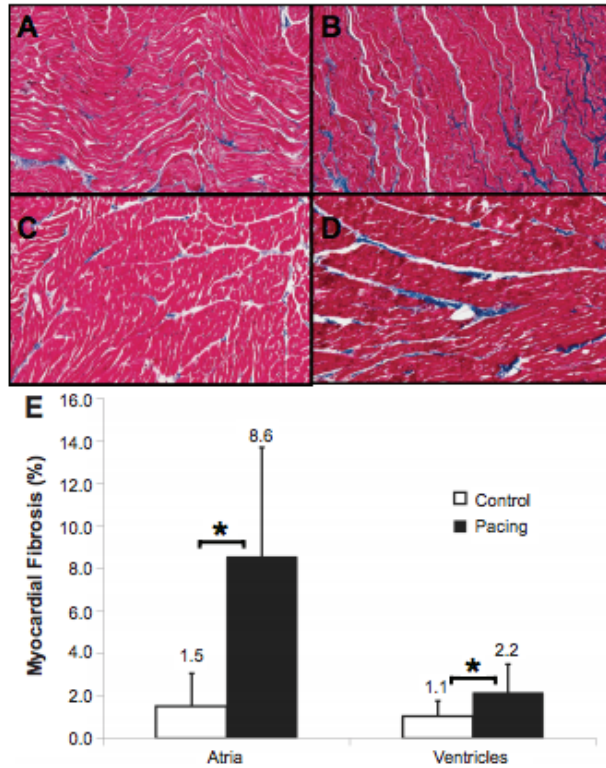
Figure 1.5: A) LA sample from control dog. B) LA sample after 6 months AF dogs. C) LV sample from control dog. D) LV sample after 6 months. E) The fibrosis increases both in the atrium and ventricle. The number indicates the SDs [39]

.

injection of the contrast agent, minimum time after which the healthy tissue eliminates the contrast medium and appears dark. The damaged cells instead appear bright white because their elimination of the contrast medium is lower (Figure 1.6). However, LGE acquisition has a main limitation: the lack of standardized image acquisition protocol. LA wall image intensity on LGE-MRI is affected by parameters such as surface coil proximity, contrast dose, delay time of image acquisiton after contrast injection and individual characteristics such
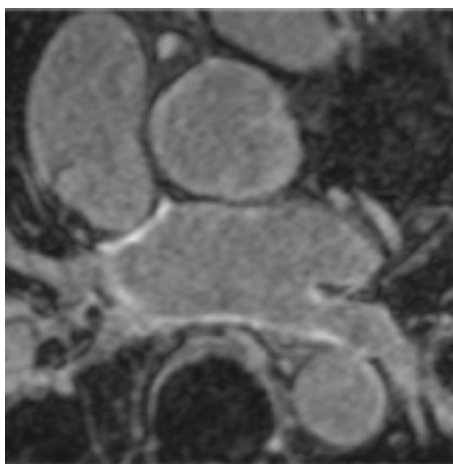
Figure 1.6: Example of a LGE-MRI acquisition. The bright region represents the fibrotic tissue on the atrial wall.

as the body mass index, renal function and haematocrit. All these technical variables can affect comparison across centres, and together with the absence of standardized image processing protocol, can lead to different results. Another problem is the image resolution and the thickness of the atria wall. While ventricular fibrosis assessment has achieved excellent results using MRI, the challenge of atrial fibrosis assessment remains open because of the limited image resolution, the atrial wall thickness and the unpredictable shape of the LA wall [40]. Therefore, a reliable and reproducible method to locate and quantify miocardial fibrosis in atrium is still lacking. In recent years, several groups tested the ability of LGE-MRI to detect both pre-existing fibrosis and post-ablation scarring [41, 42]. DECAAF study conducted by the CARMA Center, reported that extent of fibrosis my predict recurrences after the ablation procedure and therefore the information about the fibrosis exent may help the electrophysiologist in patient's selection for the ablation procedure [43].

It was a multicenter, prospective, observational cohort study of patients affected by paroxysmal and persistent AF (undergoing their first catheter ablation) conducted in 15 centers: in USA (6), Australia (1) and Europe (8). LGE-MRI

images were acquired up to 30 days before the procedure. Data acquisition was performed during the LA diastole. The other scan parameters for LGE-MRI at 3T were: voxel size=1.25x1.25x2.5 mm, TR=3.1 ms, TE=1.4 ms, flip angle=14 degrees. The same parameters for LGE-MRI acquired at 1.5T were: voxel size= 1.25x1.25x2.5 mm, TR=5.2 ms, TE=2.4 ms, flip angle=20 degrees. Each of the participating centers followed their regular clinical protocol for contrast injection for cardiac MRI.

A 3D LA patient-specific model with fibrosis distribution was obtained from the manual segmentation of the endocardial and epicardial borders. The manual tracings were achieved by an expert directly from the LGE-MRI (Figure 1.7). The fibrosis was quantified using a thresholding algorithm on grey-intensity level and it was based on image's histogram by estimating the mean and the standard deviation of "normal" tissue. "Normal" tissue was defined as the lower region of the pixel intensity histogram between 2% and 40% of the maximum intensity within the region of interest (e.g., the LA wall). The enhanced/fibrotic threshold was then calculated as two to four standard deviations above the mean of "normal." The threshold was estimated for each patient individually and the threshold was estimated slice by slice [44].

According to the fibrosis percentage, patients were classified in four groups (Figure 1.8) and the study reported the patients classified in the fourth group presented AF recurrence after the ablation procedure. The DECAAF study was the first multicenter study demonstrating the feasibility and potential clinical value of the LGE-MRI in the management of patients with AF and considered for ablation.

As mentioned in section 1.2 of this chapter, another non-invasive predictor factor of the AF recurrence is the LA enlargement. Although the casual relationship between AF and LA dilation remains controversial, it is well recognized LA enlargement is related to the presence of AF in both patients with structural heart disease and those with lone AF [45].

Some studies [46, 47, 48] have demonstrated that an enlarged LA measured by echocardiography, MRI, or CT, predicts the AF recurrence after the RFCA
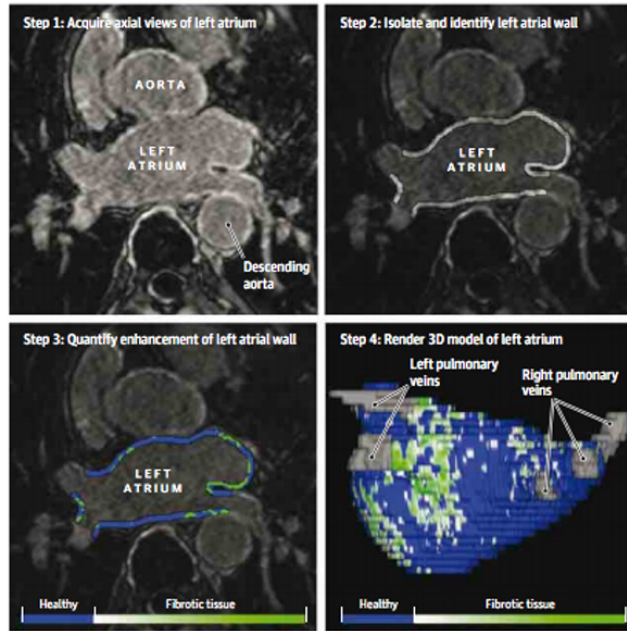
Figure 1.7: Implemented workflow for the 3D LA fibrosis model contruction. LGE-MRI acquisition (step 1). Atrial wall manually segmented (step 2). Wall segmentation includes the 3D extent of both the LA wall and the antral regions of the PVs. Quantification of fibrosis is based on relative intensity of contrast enhancement (step 3). The 3D model is rendered from the endocardial and wall segmentations and the maximum enhancement intensities are projected on the surface of the model (step 4).

and, more recent recommendations include LA size criteria for patient's selection for the ablation procedure [15]. The most widely used linear dimension is the LA anteroposterior measurement in the parasternal long-axis view using M-mode echocardiography or, preferably, 2D echocardiography [49, 50, 51]. Although this measurement has been used extensively in clinical practice and research, it has become clear that frequently it may not represent an accurate picture of LA size. Traditionally, the anteroposterior dimension was widely used because it was known to be the most reproducible measurement. However, assessment of LA size using only the anteroposterior diameter assumes that
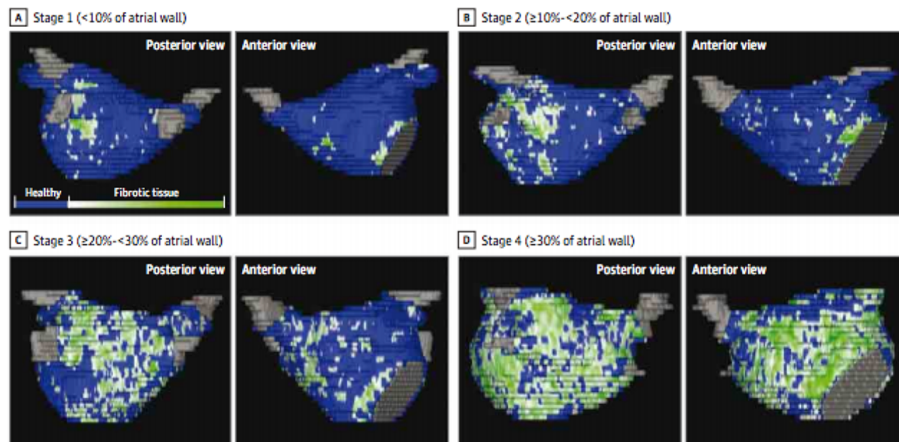
Figure 1.8: 3D rendering of the LA in four patients classified according the Utah classification. The blue region represents the healty tissue, the green and white regions the fibrotic changes. The fibrosis is expressed as a percentage of the total atrial wall volume.

when the left atrium enlarges, all its dimensions change similarly, which is often not the case during LA remodeling. When assessing the LA size and remodeling, the measurement of LA volume is recommended. Evaluation of volume takes into account alterations in LA chamber size in all directions [49, 52, 53]. Three-dimensional echocardiography holds promise for assessing LA volume and correlates with CT and MRI but the lack of a standardized methodology and limited normative data [54] are limitations to the use of 3D echocardiography.

1.3.2 Electrical remodeling

Atrial electrophysiological properties are governed by ion channels, pumps and exchangers, any of which can be altered by atrial remodeling. The principal components of electrical remodeling identified to date include decreased L-type Ca^{2+} current, rectifier background K^+ current and constitutive acetylcholine-regulated K^+ current and abormal expression (and distribution) of the gap junc-

tion connexin hemichannels that connect cardiomyocites electrically [55]. These electrophysiological changes are responsible for initiation and maintenance of AF mechanisms.

There are three main hypotheses regarding the generation and maintenance of AF:

- Multiple reentrant wavelets [56]: AF is perpetuated by continuous conduction of several independent wavelets propagating through the atria in a chaotic manner (Figure 1.9 A).

- Focal hypothesis [25]: AF is maintained by high frequency focal source near the ostia of the PVs. Fibrillatory conduction is generated when the wavefronts become fractionated and disorganized among the heterogeneous atrial tissue (Figure 1.9 B).

- Rotor hypothesis [57]: AF is generated and maintained by a stably rotating pattern (electrical spiral waves) that surrounds a pivot point (Figure 1.9 C).

The rotor theory was recently proposed by Narayan et al. [57]. The CONFIRM study was conducted using a 2D rudimental electroanatomical mapping system (RhythmView system, Abbott, ILL, USA) and using the 64-pole basket catheter (Constellation, Boston Scientific Inc., MA,USA). The Constellation catheter, considering the typical size used in clinical practice (diameter: 60 mm, covered area: 117 cm^2, intra-electrode spacing: 5 mm), once opened, is able to privide real-time mapping in just one heart cycle, acquiring simultaneous longitudinal and circumferential signals (Figure 1.10). The study enrolled 107 patients with paroxysmal and persistent AF. The subjects were divided in two groups: FIRM-guided group (36 patients) and FIRM-blinded group or conventional ablation (71 patients).

Electroanatomical AF maps were obtained during all procedures using the CARTO and NavX system; electrical rotors were localized using the RhythmView system (Figure 1.11). The study showed FIRM ablation was able to
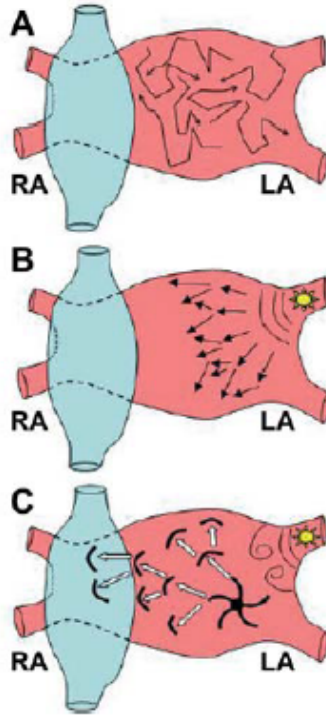
Figure 1.9: A) Multiple reentrant wavelets. B) Focal hypothesis. C) Rotor theory.

Figure 1.10: Constellation catheter (left). RhythmView system (right).
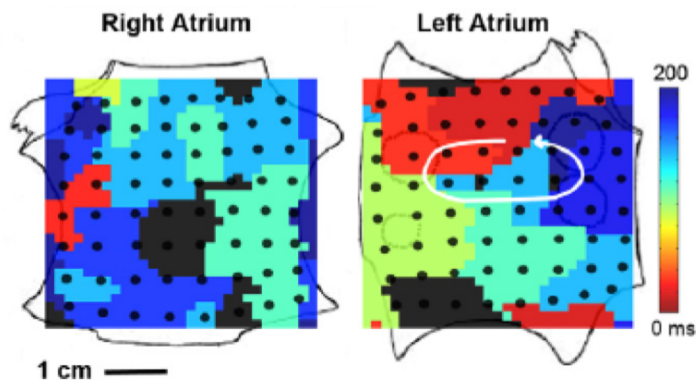
Figure 1.11: Disorganized right atrium during AF (left). LA rotor (white arrow) with counterclockwise activation (red to blue) (right).

terminate or consistentely slow persistent and paroxysmal AF before any conventional ablation in 86% of patients and substantially increase long-term AF elimination compared to the conventional ablation. The AF termination was obtained in 20/36 patients. By comparison, in the FIRM-blindend group, the acute endpoint was achieved in 20% of patients and AF termination in 6/65 patients. The CONFIRM trial demonstrated for the first time that human AF may be sustained by stable (in time and in space) electrical rotors whose ablation my improve the outcome of the ablation procedure.

Nowadays, the rotor identification as a possible targets for AF mechanisms and their stability, remain controversial. Recent studies [58, 59] demonstrated the presence of meandering rotors on the space with a very short persistance in time, other studies [60, 61] conducted with the high density mapping didn't confirm the presence of the rotors.

Another aspect not yet clarified is the role of high DF sites in the maintenance of AF. DF is the frequency occuring most often in a signal and it correspondes to the frequency where the power spectral density is maximum. In persistent AF, DF values vary in a range of [3-15] Hz. A study conducted by Sanders at al. [62], indentified sites of high frequency activity during AF with different distribution in paroxysmal and permanent AF whose ablation may improve the

success rate of the RFCA. The study comprised 32 patients undergoing AF ablation (19 paroxysmal, 13 permanent). The DF values were estimated for each EGM acquired by the mapping catheter during the ablation and the 3D DF maps were constructed. The high DF sites were defined as the maximal frequencies surrounded by a decreasing frequency gradient $\geq 20\%$ (Figure 1.12). The spatial distribution of the high DF sites in paroxysmal patients were located
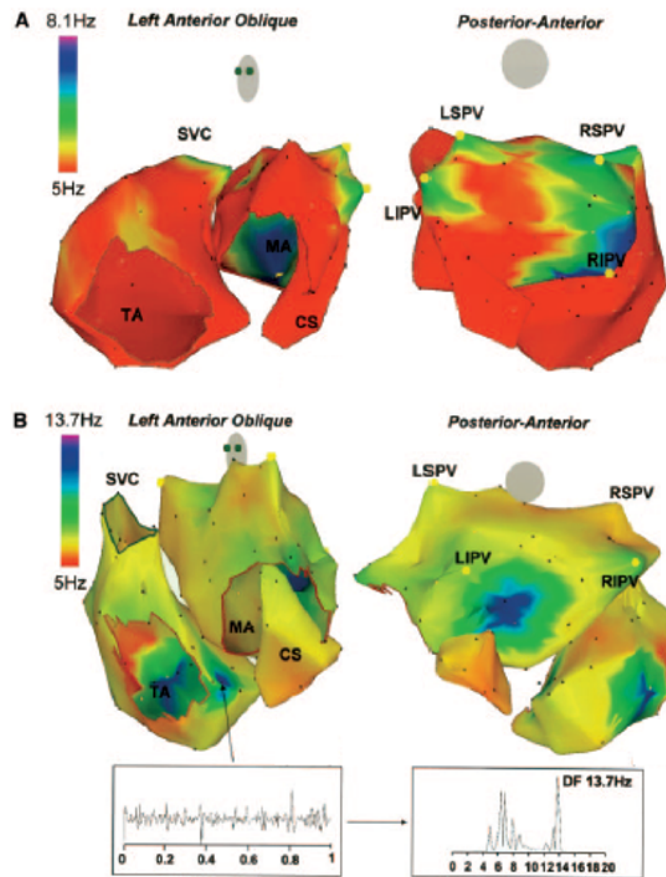
Figure 1.12: A) 3D DF maps in patient with paroxysmal AF. High DF sites are located in each PV. B) 3D DF maps in patient with permanent AF. The maximal atrial frequency (DF) is higher than the paroxysmal case. Many high DF sites are located outside the PVs.

within the PVs, whereas in the permanent AF, the sites were more prevalent and located both inside and outside the PVs. The study demontrated the ablation of the high DF sites resulted in a slowing and termination of paroxysmal AF in 87% of patients, confirming the role of localized sites of high frequency in the maintenance of AF. However, patients with permanent AF did not benefit from the DF site ablation.

1.4 Aim of the thesis

The aim of the thesis is the development of computational approaches to investigate the underlying mechanisms of AF, not yet clearly identified. In particular the PhD project is focused on a) a fully-automated approach for fibrosis quantification and LA volume estimation and on b) the development of an independent approach to examine the presence of the drifting and fast rotors that could represent the drivers of AF. Of the three main theories previuosly described about the electrical characterization of the LA in AF, this PhD thesis is focused on the electrical rotors theory, which is nowadays one of the more debated topics in the electrophysiological community.

Chapter 2

Structural characterization of the LA in AF

This chapter describes the studies carried out on the structural remodeling of the LA during AF and it is divided in two sections. In the first one, the new fully-automated approach implemented for the atrial volumetric characterization is illustrated and the results on its validation are described. The second section is focused on the automated assessment of the atrial fibrosis through the development of a 3D patient-specific LA model that integrates the anatomical and structural information and the use of several approaches for the fibrosis quantification. The implemented method was tested on the MRI data provided by the CARMA Center through a free access website.

2.1 Development of 3D patient-specific model for LA volumetric analysis to support ablation in AF patients

Content of this first section is based on the article "3D patient-specific models for left atrium characterization to support ablation in atrial fibrillation patients" by Maddalena Valinoti, Claudio Fabbri, Dario Turco, Roberto Mantovan, Antonio Pasini, Cristiana Corsi (*Magnetic Resonance Imaging*, 45:51-57,2018).

2.1.1 Introduction

It is well known that atrial enlargement is a common consequence of AF and may facilitate the induction and perpetuation of AF. Both LA diameter and volume were previously studied to determine the accuracy for LA enlargement assessment.

Over the last decade, a series of studies [63, 64] have been performed to assess the relationship between LA anteriorposterior diameter estimated with transthoracic 2D echocardiography and AF recurrence after RFCA. These studies showed inconsistent results. Abecasis et al. [65] demonstrated that LA volume was related to the outcome of radiofrequency ablation, whereas the diameter was not. LA diameter is often asymmetric and oriented predominantly in superior-inferior and medial-lateral direction underestimating the LA enlargement [66, 67]. Therefore, accurate assessment of LA volume using a three-dimensional imaging modality might be essential for the improvement of AF patient selection for RFCA.

Another aspect is the influence of the 3D LA reconstruction on the ablation outcome. Previous studies on the 3D LA reconstruction reported LA geometry is essential for RFCA ablation safety and efficacy. In the clinical setting, 3D geometries are usually obtained by a point by point EAM resulting in a rough

anatomical model of the LA including PVs. The construction of the EAM is a time-consuming, potentially imprecise and cumbersome procedure [68, 69]. Nowadays several navigation systems allow to import data from MRI or CT for a more reliable 3D LA reconstruction [70]. Both CT and MRI provide accurate anatomical LA reconstruction; however, image processing for the extraction of the 3D LA surface is manual and relies on operator expertise. In addition, with respect to CT imaging, MRI acquisition does not emit ionizing radiation and could provide additional information on fibrotic tissue on the atrial wall [71]. In this scenario, a patient-specific LA anatomical model derived from MRI, including a better identification of PVs, could assist RFA procedure. In addition, the availability of such 3D model could also provide additional informations related to patient selection for RFCA procedure, as the atrial volume.

Accordingly, this study aimed at developing a unified, fully automated approach to build a 3D patient-specific LA model including PVs in order to provide an accurate anatomical guide during RFCA and a 3D patient-specific LA model without PVs in order to characterize LA volumetry and support patient selection for AF ablation, from MRI.

2.1.2 Materials and methods

Study population and MRI acquisition The study was approved by the Ethics IRST, IRCCS AVR Committee (CEIIAV n. 1456 prot. 6076/2015 I.5/220). Twenty-six patients referred for AF RFCA were included in the study. Informed consent was obtained from all the subjects. The main clinical characteristics of patients are summarized in Table 2.1. Images were acquired with a 1.5 T MRI scanner (Achieva, Philips Medical System) and a 3D spoiled gradient recalled sequence was applied. Contrast enhanced 3D MRA images were acquired (echo time: 1.12 ms, repetition time: 3.74 ms, flip angle: 25°, in-plane resolution 0.7 x 0.7 mm and slice thickness 3 mm, with 1.5 mm overlap) with gadolinium injection of 0.1 mmol/kg followed by a 20 ml saline flush. Acquisition was ECG triggered and in breath hold.

Patient ID	Sex	Age	Weight [kg]	Height [cm]	LA size from TEE before RFA	Follow-up (time)
1	M	58	78	175	Normal	No Recurrence (15 mo)
2	M	61	61	181	Normal	No Recurrence (10 mo)
3	M	63	75	170	LA slightly enlarged	No Recurrence (18 mo)
4	M	61	73	160	LA slightly enlarged*	AF (1 mo)
5	M	71	87	170	LA slightly enlarged	No Recurrence (12 mo)
6	M	50	86	178	LA slightly enlarged**	No Recurrence (24 mo)
7	M	66	105	193	LA slightly enlarged	AF (3 mo)
8	M	52	78.5	178	LA slightly enlarged	No Recurrence (24 mo)
9	M	57	90	177	LA slightly enlarged***	No Recurrence (11 mo)
10	M	56	83	173	LA slightly enlarged	Flutter (3 mo)
11	M	57	98	165	Normal	No Recurrence (4 mo)
12	F	62	74	175	Normal	No Recurrence (11mo)
13	M	56	88	165	Normal	No Recurrence (3 mo)
14	M	73	82	180	LA slightly enlarged****	AF (12 mo)
15	M	67	81	177	Normal	AF (1 mo)
16	F	64	62	172	Normal	No Recurrence (15 mo)
17	M	60	68	179	Normal	No Recurrence (3 mo)
18	M	75	86	175	LA area 23 cm2	No Recurrence (11 mo)
19	M	47	89	187	LA slightly enlarged*****	No Recurrence (1 mo)
20	M	63	90	180	Normal	No Recurrence (14 mo)
21	M	60	82	180	Normal	AF (1 mo)
22	M	55	87	167	Normal	No Recurrence (4 mo)
23	M	51	80	165	Normal	No Recurrence (3 mo)
24	M	60	90	174	LA dilated	No Recurrence (3 mo)
25	M	70	85	178	LA slightly enlarged	No Recurrence (1 mo)
26	F	61	78	163	Normal	No Recurrence (3 mo)

Table 2.1: Patients' characteristics from medical records; *AP diameter 39 mm, area 26 cm^2, volume 89 ml; **AP diameter 42 mm, area 20 cm^2, volume 26 ml; ***AP diameter 44 mm, area 29 cm^2, volume 100 ml; ****AP diameter 46 mm, area 29 cm^2, volume 100 ml; *****AP diameter 45 mm.

MRA data processing The fully automated workflow for 3D patient-specific LA model with and without PVs is shown in Figure 2.1. The first step was the
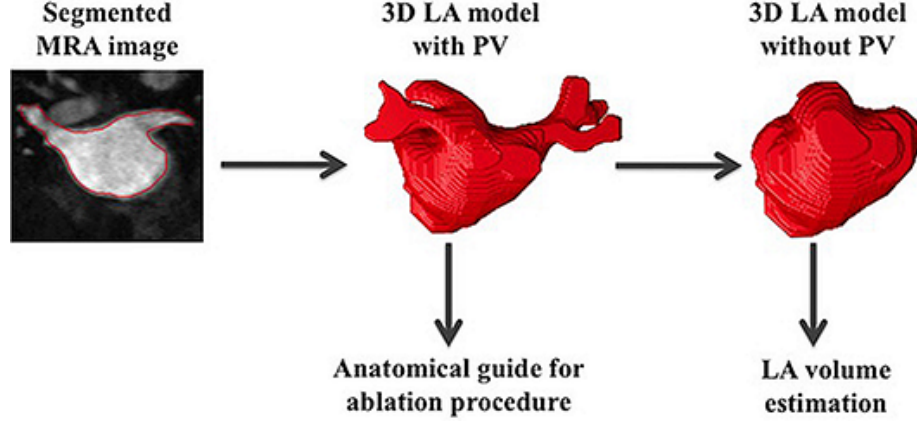
Figure 2.1: Workflow of the developed approach for 3D patient specific LA model with and without PVs. Left panel: final detected contour in a 2D MRA image; middle panel: 3D patient-specific LA model including PVs; right panel: 3D patient-specific model without PVs.

segmentation of the LA from MRA images (Figure 2.2, a). The proposed method is based on a 2D edge-based level set approach [72] guided by a phase–based edge detector. The differential equation that guides the evolution of the zero level of the level set function (ϕ) is composed by the smoothing term, the baloon term (or expansion term) and the advection term, that attracts the curve towards the edge of the image.

$$
\begin{cases}
\frac{\partial \Phi}{\partial t} = g(\epsilon K - 1)\nabla\Phi + v\nabla\Phi\nabla g \\
\Phi(x,y,t) = min(\Phi_0) \qquad\qquad\qquad\quad \nu,\epsilon > 0 \\
\Phi(x,y,0) = \Phi_0(x,y)
\end{cases}
$$

where g is the edge indicator, $g\epsilon K\nabla\Phi$ represents the smoothing term, $g\nabla\Phi$ is the expansion term, $\nu\nabla\Phi\nabla g$ is the advection term. The novelty of the implemented approach is the edge indicator, which is based on the feature asimmetry (FA)

37
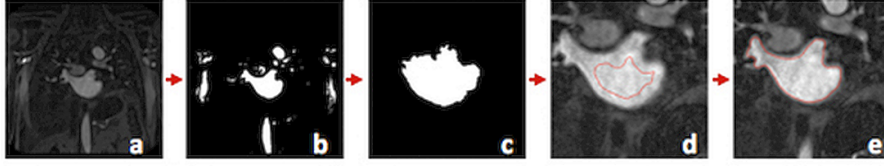
Figure 2.2: Description of the fully automated segmentation algorithm. a) An example of the MRA image. b) Result of the Otsu's method application. c) Isolation of the atrium from the other regions after the application of morphological operators and considering the atrium size end its position in the image. According to the MRA acquisition protocol, the images are acquired in frontal view and the atrium is always located in the center of the acquired images. In our approach, we took advantages from this standard procedure and the atrium is automatically selected as the region with the centroid closer to the center of the image. d) The initial condition of the level set function is automatically built considering the contour of the selected region. e) Result of the application of the segmentation algorithm.

containing the phase information of the image.

$$g = 1 - FA^{\alpha}$$

where α=1.5

FA is obtained by the monogenic signal ($f_m(x,y,z)$), which is an extension in N - dimension of the AS [73]. The monogenic signal is a complex signal derived by summing to the signal ($f(x,y,z)$), its Riesz's transform (f_R).

$$f_m(x, y) = even + i * \mathbf{odd}$$

Riesz's transform provides the imaginary components of the monogenic signal that is obtained applying odd quadrature filters. The expression of FA is obtained from the output of the filters and represents the phase congruency

(Figure 2.3).

$$FA = \frac{|odd| - |even| - T}{\sqrt{even^2 + odd^2 + \epsilon}} \qquad \epsilon > 0$$

T is a corrective costant number used to reduce the noise and artifacts, odd and even are the output of the filters. This method is characterized by a high robustness to the noise than the classic level set approach, whose edge indicator is based on the grey intensity level gradient. The initialization of the level
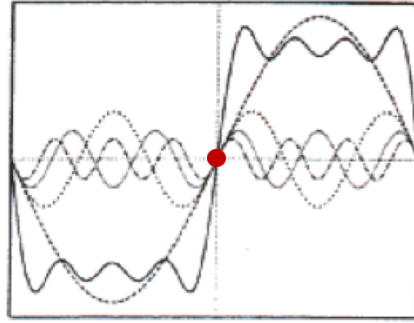
Figure 2.3: Phase information in each direction (N-domain). The red dot represents the phase congruency.

set function was obtained by applying Otsu's method [72] resulting in a rough detection of LA boundaries (Figure 2.2, b). The atrium was automatically selected applying morphological operators and considering the size of the atrium and its position in the image (Figure 2.2, c).

The distance function of the selected region was built and its zero level was used as the initial condition (Figure 2.2, d) for the evolution of the level set function. The final detected contour represents the LA endocardial boundaries including the PVs (Figure 2.2, e).

This last step also allowed to exclude the left ventricle from the final boundaries. This approach was automatically applied to all 2D MRA acquired slices in which LA was visible. From the collection of 2D detected LA contours including the PVs, the 3D patient-specific LA model was obtained (Figure 2.4).

According to the American Society of Echocardiography [49] to compute the LA volume, PVs were removed from the 3D surface previously obtained by the
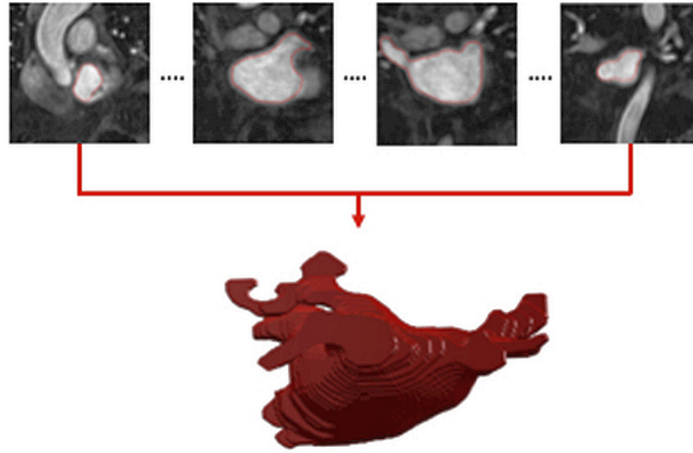
Figure 2.4: An example of 3D patient-specific LA model derived from the segmentation step. Top panel: 2D detected LA contours including the PVs. Bottom panel: 3D patient-specific LA surface derived from the segmented MRA images.

segmentation method. For this purpose the shape diameter function (SDF) was estimated.

The SDF is a scalar function defined on the mesh surface that measures the corresponding local object diameter. For each facet, several rays are sampled in a cone constructed using the centroid of the facet apex and inward-normal of the facet as axis. Each ray is truncated into a segment, its endpoints being the apex of the cone and the first mesh facet intersection point. Using the weighted average lengths of these truncated rays, which intuitively correspond to a local volume sampling, the raw SDF value is computed (Figure 2.5). The SDF was calculated for each facet of the 3D surface using the CGAL software (Figure 2.6, a). Based on the histogram of the SDF we computed the optimal threshold in order to obtain a semantic clusterization of our 3D model.

This step allowed to identify the PVs, Auricola, LA chamber and Mitral valve (Figure 2.6, b) By considering the information about PVs anatomical position, they were automatically identified and removed from the surface (Figure 2.6,
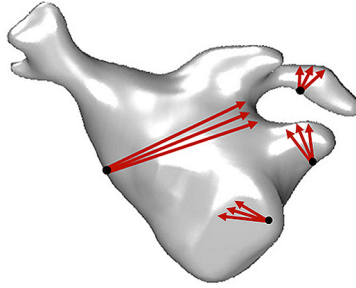
Figure 2.5: Shape diameter function. Several rays are sampled inside the cone. The lengths of the rays inside the atrial chamber are longer than ones inside the cavity (PVs, Auricola, Mitral valve).
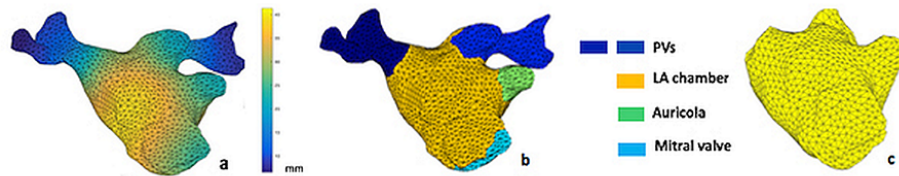
Figure 2.6: Workflow developed for the PVs identification and removal. a) SDF estimation for each facet of the 3D mesh; b) Clusterization step based on a SDF thresholding; c) Identification of the PVs considering their anatomical position on the 3D surface; d) PVs removal.

c).

2.1.3 Statistical analysis and results

The normality distribution of variables was tested using Kolmogorov-Smirnov test. All variables were not normal. Depending on the distribution, continuous variables were expressed as mean±standard deviation or median and interquartile range. Paired variables were compared using the Kruskal–Wallis test. $P<0.05$ was considered significant. One experienced investigator manually segmented LA chamber without the PVs in the MRA images of all subjects.

In order to perform manual contouring, an in-house toolbox for manual segmentation was implemented. To investigate the intra-observer variability of the manual segmentation, the analysis was repeated twice by the same investigator two months after the first tracing in 10 randomly selected patients. For each patient, the automatic segmentation results were compared with the manual segmentation in terms of surface-to-surface distance, computed as the average distance (in mm) of each automatically detected surface point to reference surface. In addition, LA volume estimates were compared with LA reference volume values by linear regression and Bland-Altman analysis. The intra-observer variability expressed in percentage, was assessed as the ratio between the difference between the two estimates and their mean value. The automatic algorithm and the toolbox for manual segmentation were developed in Matlab environment (v. R2016a, Mathworks, Natick, MA).

Automatic segmentation was feasible in all study subjects. Time required for the analysis was about 4 min for the 3D LA model with PVs and about 8 min for the 3D LA model without PVs on a 2.5 GHz, Intel Core i5 computer with 8 GB RAM. Median LA volume was 92.5 ml (ICQ (interval quartile range): 84–100 ml) from manual analysis and 92.3 ml (ICQ: 85–99 ml) from the automated approach. Qualitative comparison between the obtained 3D LA models with the point by point maps was performed and the result reported in Figure 2.7 highlights PVs reconstruction was not accurate and left atrial appendage is missing. An example of the 3D patient-specific LA models with (grey surface) and without (red surface) PVs superimposed is shown in Figure 2.8. In Figure 2.9 the comparison between manual and automated LA boundary detection in one acquired slice is illustrated. Results of the regression and Bland-Altman analyses between LA volume estimates and corresponding references are shown in Figure 2.10 (y=1.03x-1.4; r=0.99; bias: -1.37 ml corresponding to -1.43%; SD: 54.3 ml; mean percentage difference was -1.3%±2.1%; mean percentage absolute difference resulted in -1.9%±1.6%). The surface-to-surface distance was 2.3%±0.7% mm. The intra-observer variability was 2.7%±3.9% for the manual tracing performed by the expert radiologist. Since no manual interaction is re-

. Considering our experience in the EP lab, most of AF ablation procedures are guided by 3D LA models obtained applying semi-automatic segmentation algorithms on CT or MRI acquisitions. An accurate reconstruction of the LA using the point-by-point mapping is still time consuming considering the procedural time duration.
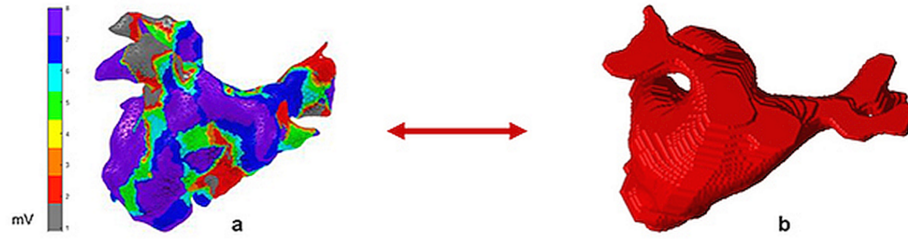
Figure 2.7: Comparison between the EAM and the 3D patient-specific LA surface. a) EAM reconstructed by the navigation system during the ablation procedure. b) 3D patient-specific LA model derived from the segmented data.

quired for the computation of the 3D LA models, LA volumes did not change when the analysis was repeated.
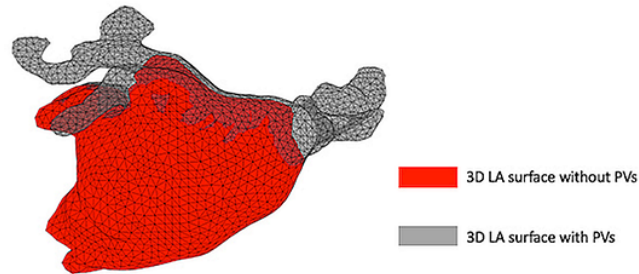
Figure 2.8: Overlapping between the 3D LA surface with PVs (grey) and without PVs (red).
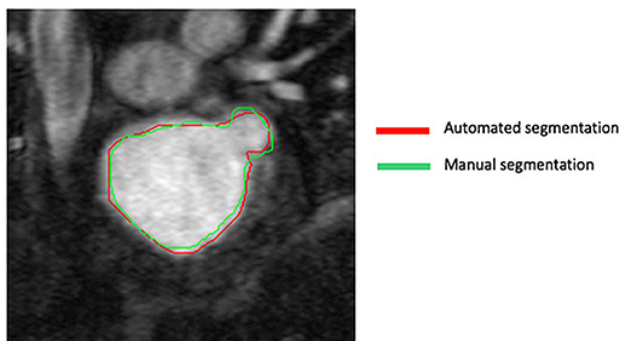
Figure 2.9: Comparison between manual (green) and automated left (red) atrial boundaries detection.
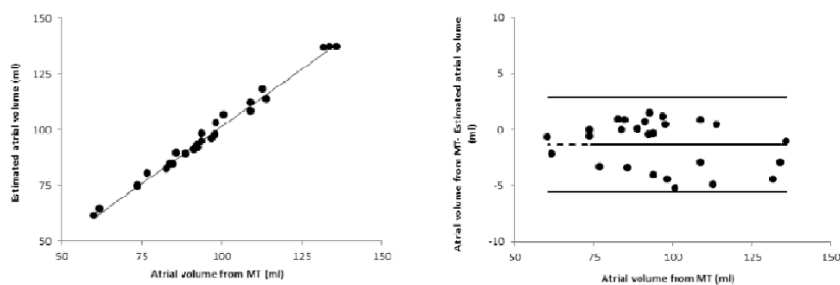
Figure 2.10: Comparison between the volumes estimated with the automated approach with ones estimated by manual tracing (MT). Results of the regression (a) and Bland-Altman analysis (b).

2.1.4 Discussion and conclusions

In AF patients, an accurate 3D patient-specific model could assist RFCA improving ablation outcome and, at the same time, provide quantitative information regarding LA volumetry which is predictive of AF recurrence. The present study proposes a unified and fast workflow allowing computation of 3D patient-specific LA models (with and without PVs) useful to support patient selection for RFCA and a reliable guidance during the therapy. A local segmentation approach based on an image phase-driven information was combined with a re-

gion based initialization for the level set evolution. The implemented method was effective and provided reliable 3D LA patient-specific models even in presence of large morphological variations, as expected considering LA anatomy. Preliminary comparison between EAMs and the 3D patient-specific LA models with PVs showed the latter are able to better describe LA anatomy. The possibility of mapping the information acquired during the ablation procedure (electrograms or EGMs and voltages) on a realistic 3D patient-specific anatomy provides a better understanding of the conduction properties of the tissue.

A detailed description of the LA anatomy especially in correspondence of PVs that represent the main target of RFA and are geometrically complex structures difficult to be accurately acquired by a point by point mapping, would allow the correct location of EGMs and voltage information on the LA wall and consequently may help in optimizing the selection of ablation sites and in evaluating RFCA acute efficacy and safety. An accurate LA anatomy would also facilitate LA navigation and thus reducing fluoroscopic time during RFCA.

Quantitative assessment of LA volume resulted in accurate and reliable estimates that are not affected by observer variability. Manual and automatic LA segmentation were in high agreement and slight differences in LA volumes computation were found applying the two techniques. As a standard procedure, LA volumes computed from manual segmentation were used as reference values to evaluate our approach. Obviously we cannot exclude inaccuracies in manual segmentation and to limit their influence, tracings were performed by an expert radiologist. In addition, to quantify this potential source of error we computed intra-observer variability. LA segmentation is a challenging task due to high variability in LA anatomy.

The proposed approach for LA volume computation is fully automated and no prior information is required. The first step of the segmentation provides a 3D LA patient-specific-model with PVs whose inclusion is mandatory for ablation guidance and voltage or activation mapping. The detection and removal of PVs detection is required for LA volume computation. Indeed, PVs removal from 3D patient-specific model was effective, since results on studied popula-

45

tion show volume computation is accurate with tight limits of agreement and small percentage errors. Only few approaches have been proposed in literature for LA volume quantification; these approaches are semi-automatic and require operator corrections [65, 74, 75]. The segmentation technique proposed by Tao [76] is based on a multiatlas dictionary by manual annotation of LA chamber and PVs. Following the multiatlas creation, the LA segmentation of a specific patient is automatic. The method requires 15 min to compute the 3D LA volume compared to 4 min of our approach. In both cases, the methods can be applied offline since no manual interaction is required. A very recent study [77] proposed a hybrid approach for fully automatic segmentation of the LA from cardiac volumetric MRI. Random forests for tissue classification followed by an active contour evolution for segmentation refinement were applied to obtain an accurate LA model with PVs. Final segmentation outperforms other methods reported in literature but computational time is about 7.5 h mainly due to random forest parallel training. The new approach showed comparable performance, slightly minor (surface to surface: 1.14±1.21 mm) with a computational time compatible with clinical application. In this study data from MRI were used. Advantages on the use of MR data versus CT and echo have been reported elsewhere showing echocardiography underestimates LA volume compared to other imaging modalities [74, 78]. The majority of studies [75, 79] aimed at LA volume quantification in AF patients used data from CT imaging and only very few studies [76] were carried out using MR images. As previously reported in [76] the use of MRA data improves segmentation accuracy and robustness without significantly affecting acquisition time and allowing the additional acquisition of late gadolinium enhanced images (LGE-MRI) from which fibrotic tissue information is readily available. Nowadays, several authors [80] proposed an atrial fibrosis-based approach for AF ablation, making this acquisition technique crucial in this specific clinical setting. The proposed 3D LA model with PVs could be easily integrated with fibrosis information by simply registering the two datasets and using grey-level intensities from LGE-MRI as a texture of the 3D anatomical model. LA volume has been shown to be a useful

index to identify patients in whom successful AF ablation can be achieved [65]. This volumetric index was proven to be associated with presence and chronicity of AF, differently from LA diameter [78, 81]. Therefore an accurate method to quantify LA enlargement seems pivotal in AF risk stratification. The proposed 3D patient-specific models for LA characterization to support ablation in AF patients has several limitations. The study population is comparably small and further validation on a large number of patients should be performed. The hypothesis that a more realistic LA anatomy detection could improve RFCA procedure, should be verified by the integration of the 3D patient-specific LA model from MRA with EGMs and voltage information acquired during ablation procedure. In addition, post RFCA quantitative data to evaluate a possible correlation between LA volume and RFCA outcome were not available.

2.2   LA fibrotic tissue assessment

Recently, LGE–MRI has been proposed to optimize AF diagnosis and treatment through the assessment of atrial fibrosis, which is considered an arrhythmogenic substrate. Several studies [43, 82] have suggested both extensive atrial tissue fibrosis and association between scar gaps and PV reconnection sites as possible causes of the poor outcomes of the AF catheter ablation. In order to assist the electrophysiologist in patient selction and ablation procedure planning, an automated approach for 3D visualization of the fibrotic tissue extent and its quantification was developed. For this purpose, LGE-MRI data were acquired on the twenty-six patients (Table 3.1) and the grey intensity levels were superimposed on the reconstructed 3D LA model obtained segmenting the MRA images. Finally, different methods were used for the fibrosis quantification and for patients' classification and the obtained results were compared in order to investigate if Utah classification may depends on the method applied to quantify the fibrosis extent.

2.2.1 Materials and methods

The LGE-MRI data were acquired with the same scanner used for the MRA acquisitions. 3D MP-inversion recovery with fat saturation was applied (echo time: 3.20 ms; repetition time: 6.52 ms; flip angle: $22°$, 3 mm thick, 1.5 mm overlap in-plane axial spatial resolution: 0.95 mm; scan time: 15-20 min depending on HR and respiration). The images were acquired 15 min after contrast injection. An example of the DE-MRI image is shown in the Figure 2.11. The structural
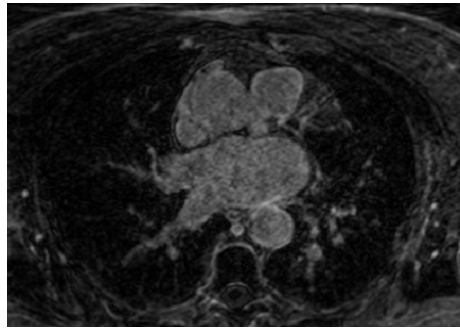
Figure 2.11: Example of an acquired LGE-MRI image.

remodeling information derived from LGE-MRI data was superimposed on the 3D LA model applying a multimodality affine registration on the data based on mutual information (MI) as a similarity measure (Figure 2.12) [83, 84, 85]. More specifically, the MRA images were registered in the spatial domain of the LGE-MRI and the estimated affine matrix was then used to register the 3D LA patient-specific model in the LGE-MRI spatial domain (Figure 2.13). Before the registration, the axial view of the MRA images was reconstructed.

The corresponding intensity grey level information derived from the LGE-MRI (Figure 2.14, (a)) was used as a texture (Figure 2.14,(c)) on the registered 3D surface LA model obtained from the MRA segmentation (Figure 2.14,(b)), allowing the 3D visualization of LA fibrosis location and extent (Figure 2.14,(d)). The 3D model obtained is able to provide the real fibrosis tissue distribution and its extension on the wall.

48
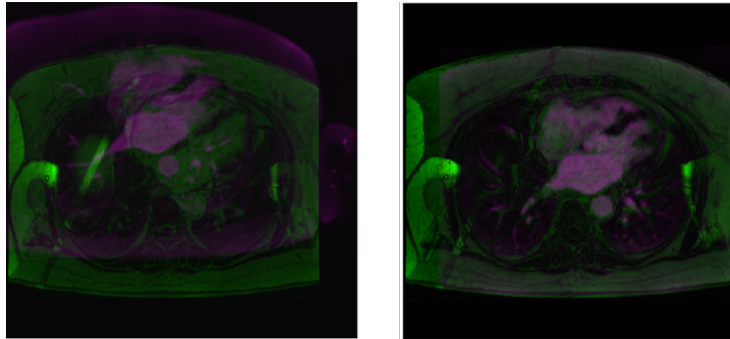
Figure 2.12: MRA (purple image) superimposed on LGE-MRI (green image) before (left) and after (right) the registration.
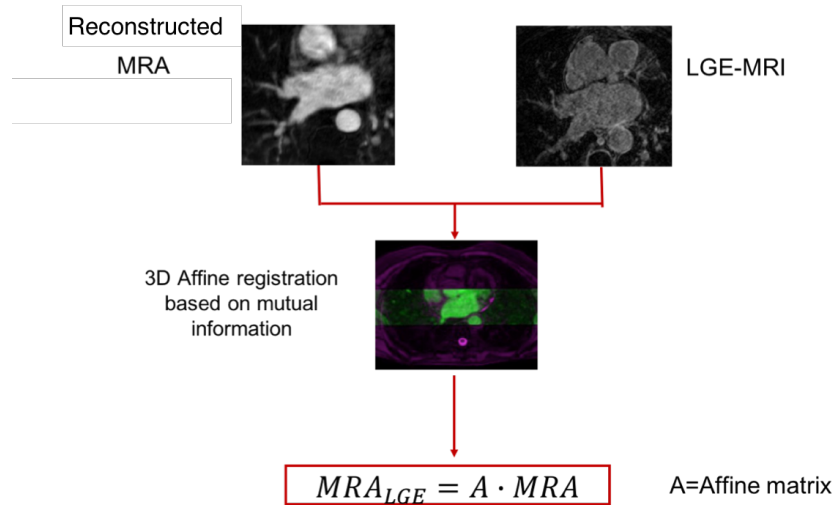
Figure 2.13: Workflow of the registration step

The last step of the implemented workflow regards the fibrosis quantification. The employed methods are described below.

Histogram-based reference This thresholding technique is based on the histogram of the image. Normal tissue is defined automatically as the mean of the lower region of the pixel intensity histogram (between 2 and 40% of the
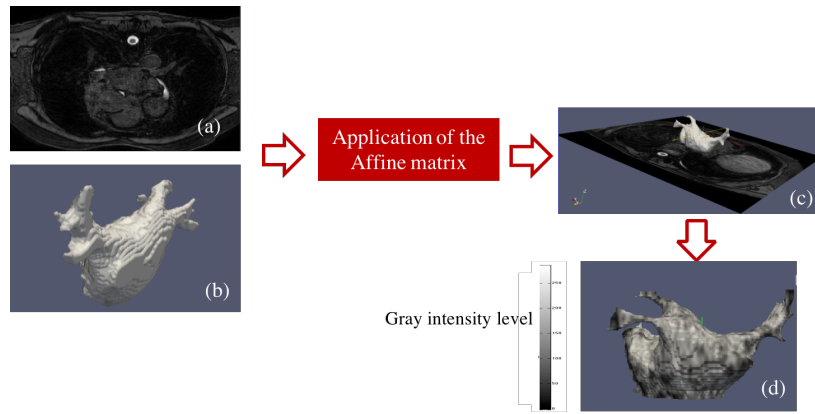
Figure 2.14: Schematic reconstruction of the 3D LA model with fibrosis distribution superimposed.

maximum intensity within the LA wall). The threshold cut-off to detect the fibrotic tissue is chosen at 2-4 SD above the mean of the normal tissue value (Figure 2.15) [44]. Mathematically, it can be written as:

$$Th_{\text{fibrosis}} = M_{\text{NT}} + N \cdot SD_{\text{NT}}$$

where M_{NT} and SD_{NT} are the mean and standard deviation of the normal tissue.
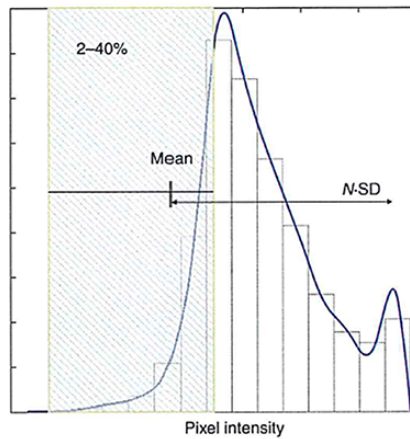
Figure 2.15: Histogram-based reference

Image intensity ratio   The image intensity ratio (IIR) is a normalized measure to assess LA fibrotic tissue on LGE-MRI. The IIR normalizes myocardial image intensities by the mean blood-pool intensity [40]. The IIR equation is the following:

$$IIR = \frac{SI}{MP_{\mathrm{BP}}}$$

where SI is the signal intensity, and M_{BP} is the mean of the blood-pool. Dewire et al. [86] used this method to detect pre-existent LA fibrosis and they distinguished normal tissue (IIR<0.97), abnormal myocardium (0.97<IIR<1.21), fibrotic tissue (1.21<IIR<1.61) and dense scar (IIR>1.61).

Fibrotic tissue segmentation using graph cut   The graph cut is a method used for image segmentation that can be formulated in terms of energy minimization. "Binary" problems can be solved exactly using this approach; problems where pixels can be labeled with more than two different labels cannot be solved exactly, but the solutions are usually near the global optimum. The output of the graph cut method is a binary data. A graph is a representation of a set of objects, where several pairs of the objects are connected by links. In this project, this method was used to segment the fibrotic tissue by treating each pixel in the image as a node of the graph. Apart from these nodes, the graph is composed by other extra nodes called "terminal nodes", each representing an object in the image. All the pixels are connected to all their adjacent pixels and to the object nodes. In the binary problems, two terminal nodes, called background terminal and object terminal are used (Figure 2.16). For the fibrosis segmentation, the two terminal nodes were defined as healthy myocardium and fibrotic tissue, analogous to the image background and foreground of general image segmentation problems.

In a graph $G = (V, E)$, V and E denote the set of vertices and edges of G, respectively. For the fibrosis segmentation we can consider a weighted graph with two distinguished verticals terminal nodes. A cut $C \subset E$ is a set of edges such

(a) Image with seeds.   (d) Segmentation results.

(b) Graph.   (c) Cut.

Figure 2.16: A schematic implementation of the graph cut methods.

that the terminal nodes are separated in the induced graph $G(C) = (V, E - C)$. The cost $|C|$ of the cut C is defined as the sum of its edges weights. It is possible to consider each image voxel as a node in the graph and each of the voxel nodes has edges that connect it to its neighbors (N-links), and the two terminal nodes (T-links) [87].

A minimal cut generates a segmentation that depends on the definition of the edge weights and on the choice of the energy function.

The energy function (EF) is defined as:

$$EF(L) = \lambda \underbrace{\sum_{x \in X} R_x(L_x)}_{\text{regional term}} + (1 - \lambda) \underbrace{\sum_{(x,y) \in N} B_{xy}(L_x, L_y)}_{\text{boundary term}}$$

where $L = L_x | x \in X$ denotes a segmentation, X is the voxel set, N is the

52

neighboring relations on the voxels. R_x is the regional term, which evalutes the fit of the class membership (fibrotic tissue or healthy tissue) to the data voxel intensities. R_x was obtained from the Gaussian mixture model to set the regional term weights:

$$R_x("healthy") = -lnP("healthy"|I_x) = -ln\left(\frac{\pi_1 N(I_x|\mu_1, \sum_1)}{p(I_x)}\right)$$

$$R_x("infarct") = -lnP("infarct"|I_x) = -ln\left(\frac{\pi_2 N(I_x|\mu_2, \sum_2)}{p(I_x)}\right)$$

where, I_x is the intensity at voxel x, π is mixture weighting coefficients, μ is the mean intensity inside the healthy/fibrotic region, , $\sum_k$ is the covariance matrix, $N(\cdot)$ is the Gaussian probability distribution. The boundary term B_{xy} evaluates the penalty for edges between pixels (8-way connected neighborhood), and it is defined as:

$$B_{xy}(Lx, L_y) = \frac{e^{-\beta||I_x - I_y||^2}}{dist(x, y)}$$

where, dist(x, y) is the Euclidean distance between voxel x and y, and β is the penalty coefficient [87].

2.2.2 Results

The difficulties on LGE-MRI data acquisition not allowed a correct visualization of the fibrotic tissue on the atrial wall in most of the data. Both healthy and fibrotic tissue appear bright white in the images (Figure 2.17) and for this reason the previously described models were tested on MRI data of DECAAF study [43] provided by the CARMA Center thorough a free- access website.

The automated workflow for the fibrosis assessment was tested on ten patients affected by AF. In-plane axial spatial resolution of both MRA and LGE-MRI data is 0.65x0.65. The slice thickness was 1.25 mm (Figure 2.18) with no gap or overlap between slices. The other scan parameters are described in Chapter 1. Before segmentation, the MRA data were in the axial view. Registration was
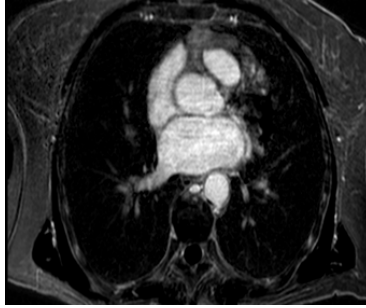
Figure 2.17: An example of LGE-MRI in which both healthy and fibrotic tissue appears bright white.
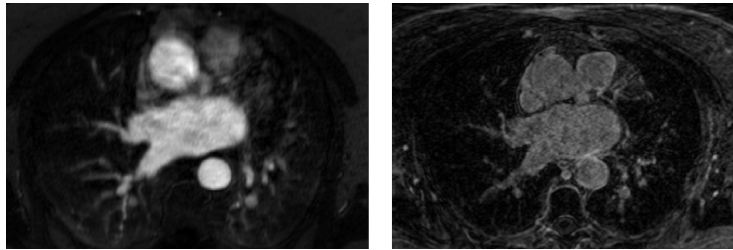
Figure 2.18: An example of MRA image (left) and LGE-MRI (right).

applied to MRI data in axial view and the estimated affine matrix was used to register the 3D LA surface obtained from the segmentation on the LGE-MRI spatial domain. Finally, the grey intensity levels of the LGE-MRI were superimposed on the 3D model and the fibrosis was quantified (Figure 2.19).

Each quantification method was applied to the LA wall. The epicardium identification was obtained applying the dilation operation to the endocardium contours, taking into account the LA wall thickness.

Time required for the total analysis (from the MRA segmentation to the fibrosis quantification) was about 15 min. The results of the fibrosis quantification estimated using the methods previously described are reported in the Table 2.2. In addition, patients were assigned to 1 of 4 groups (fibrosis stages 1-4) according to the Utah classification.

As in the DECAAF study, the overall volume of the LA myocardium was calcu-
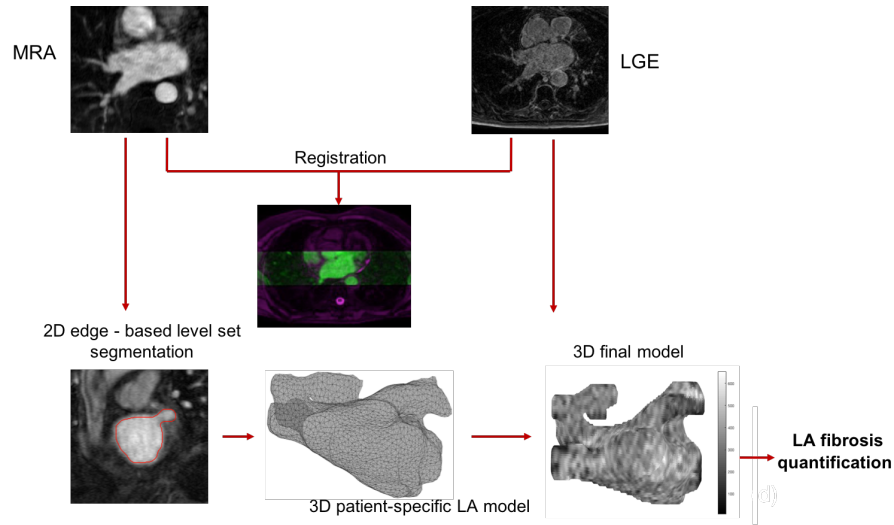
Figure 2.19: Application of the implemented workflow for the fibrosis assessment on the CARMA Center data.

lated as the number of the voxels within the endocardial and epicardial contours. The extent of enhancement was then computed as the number of the pixels identified as enhanced by the methods over the volume of the LA myocardium for the slice.

A qualitative result of the application of the graph cut method for the fibrosis segmentation in one slice is shown in the Figure 2.20. An example of the volu-
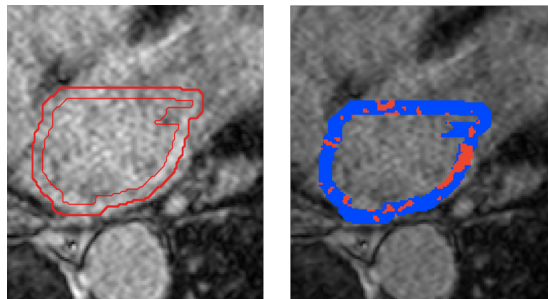
Figure 2.20: Example of the result of the fibrosis segmentation (red regions) on the LA wall obtained using the graph cut (right) in one slice (left). The blue region represents the healthy tissue.

metric percentage of the LA wall enhancement estimated by the three methods in one patient is shown in the Figure 2.21.
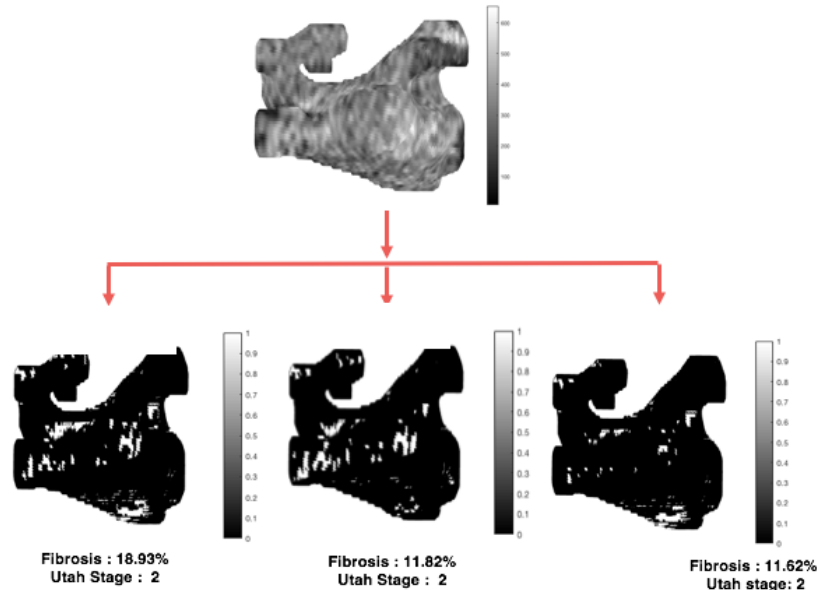
Figure 2.21: top panel) 3D LA model obtained in one patient with the fibrosis information superimposed. Binary maps (bottom panel) that show the fibrosis percentage (white regions) on the 3D atrial surface estimated with the histogram based reference method (left), with the IIR method (middle) and using the graph cut for the fibrosis segmentation algorithm (right). In this example all methods classified the patient in the Utah 2, despite the difference on percentage of fibrosis estimation.

2.2.3 Conclusion and discussion

An automated approach for 3D visualization of the fibrotic tissue extent and its quantification was developed. The implemented workflow was tested on ten MRI data acquired at the CARMA Center that were assigned to 1 of 4 groups (fibrosis stages 1-4) according to the Utah classification.

Up to now no methods can be defined as "gold standard" for the fibrosis quantification and this work highlighted the Utah classification strictly depend on the selected method for the analysis. The IIR method detects smaller areas of fibrosis than the other ones whose performance are similar. Since, the classification of the tissue as normal, abnormal, fibrotic or dense scar was performed following [86] and the image acquisition protocol is not standardized, this may result in incorrect classification results. Unfortunately the availability of only few data did not allow us to define different thresholds. In most cases, patients' classification performed using the histogram-based reference method is the same to the classification computed using the graph cut. The Mann-Whitney test was performed and the statistical test showed the two classifications are not statistically different (π¡0.05).

Another important aspect is the correct segmentation of the LA wall. In the DECAAF study the LA wall segmentation is manually traced by an expert but the LA wall detection might be affected by the intra/inter observer variability. Several methods have been developed automatically to quantify the LA wall thickness from CT images. In [88], a segmentation of the wall in four regions, inter-atrial septum, below right inferior pulmonary vein, appendage and anterior wall was performed whereas [89, 90] chose to build a pipeline based on a multiregion segmentation method. However this task remains challenging, because the LA wall is heterogeneous, thin, consisting of mix of granules and fibrosis, especially in patients with myocardial diseases or persistent AF. Moreover, the accuracy of the segmentation is also difficult to validate, as few manual segmentations or reliable ground truths are available [91].

The results of the fibrosis quantification require further validation on a larger population. However, based on our experience acquisition of LGE-MRI, strongly relies on the radiologists experience and the merely application of the protocol proposed in the DECAAF study does not directly imply good quality images.

Patient	Histogram-based reference		IIR method		Graph-cut approach	
	fibrosis (%)	Utah Stage	fibrosis (%)	Utah Stage	fibrosis (%)	Utah Stage
#1	18.98	2	5.64	1	8.54	2
#2	31.55	3	6.31	1	21.77	3
#3	34.88	3	16.07	2	22.51	3
#4	18.93	2	15.72	2	11.62	2
#5	16.67	2	8.97	1	8.31	2
#6	43.56	4	2.70	1	26.07	3
#7	43.92	4	9.63	1	30.13	3
#8	24.94	3	8.92	1	12.65	2
#9	14.97	2	4.91	1	6.05	2
#10	24.70	3	4.55	1	13.45	2

Table 2.2: Results of the fibrosis percentage estimation and patients' classification obtained with the three methods. In this work, 5 SD was used in the first method, and the threshold used to define the fibrotic tissue in the second one was: 1.20<th<1.61. In the graph cut, β was 5, to increase the relative importance of high gradient between pixels of different class and λ was 0.5.

Chapter 3

Electrical characterization of the LA in AF

In this chapter the methods designed and developed to characterize the LA electrical activity are illustrated. In particular a new approach for the meandering and stable rotor localization and detection on the 3D LA surface is described and the results of its validation are showed. In addition, the use of different catheters to acquire EGMs allowed us to derive some considerations about their ability to map the LA and detect AF triggers.

Rotor ablation guided by the basket catheter mapping has shown to be beneficial for AF ablation [57]. Yet, the initial excitement was mitigated by a growing skepticism due to the difficulty in verifying the protocol employed by the RhythmView® system in locating electrical rotors. Overall, the underlying assumptions of the FIRM protocol still need verification: i) AF is sustained by stable rotors; ii) a rotor can be terminated by ablating its core; iii) the basket catheter allows reliable rotor mapping. In this chapter, a fully-automated workflow for the rotor detection on the LA surface, based on the phase analysis of the EGMs is described. The workflow was divided in two steps, oppurtunely vali-

dated. The first one was the LAAT detection and 3D phase map construction. For the LAAT localization on the EGMs a modified version of the SR method [92] was implemented in order to improve its outcome. The developed approach was validated using synthetic EGMs and their construction is illustrated in the section 3.1.2.1. The second step was the development of the meandering and stable rotor detection algorithm and its performance was tested using an atrial computational model published in literature. In addition the persistence in time of the detected rotors was computed. Finally, in order to verify the efficacy of the basket catheter and its spatial coverage on the rotor detection, its performance was compared with another catheter with a spatial resolution lower than the Constellation.

3.1 Clinical data

Six patients with paroxysmal AF, aged 37 to 75 were enrolled in the study at "M. Bufalini" Hospital, Cesena, Italy. All patients underwent an ablation procedure and the Constellation catheter was used to acquire unipolar EGMs. The registrations are 10s long and the sampling frequency is 2000 Hz. Digital electro-anatomic atrial shells were created for clinical guidance using the NavX mapping system.
The study was approved by the Ethics IRST, IRCCS AVR Committee (CEIIAV n. 1456 prot. 6076/2015 I.5/220) and informed consent was obtained from all the subjects.

3.2 LAAT detection algorithm and phase map construction

Since it is well known [93] that the main problem of the basket catheter is its coverage of the endoatrial wall, for the detection of LAAT we discarded the

EGMs acquired by the electrodes whose position was farther than 13 mm from the LA wall. This threshold was empirically fixed considering the electrophysiologist's suggestion.

The remaining EGMs were band-pass filtered (3 to 80 Hz) and far-field QRS complexes were subtracted from the unipolar EGMs by a single-beat cancellation method [94]. A template of the ventricular far-field potential was obtained by averaging all time windows of the LA EGMs around R-wave peaks detected in the ECG signals (Figure 3.1). The R-wave peak detection algorithm is based
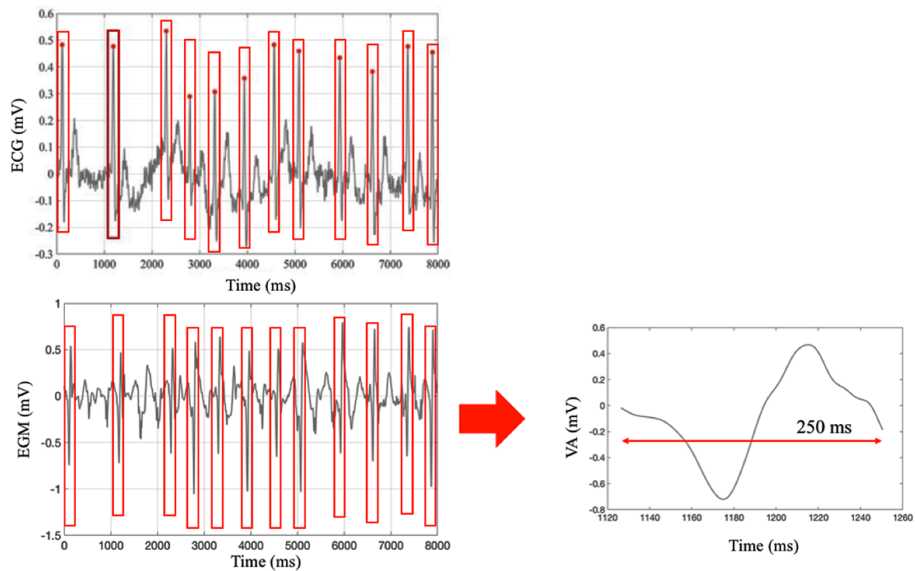
Figure 3.1: Ventricular template estimation. Top panel: ECG signal with the detcted R-wave peak (red dots). Ventricular template was obtained by averaging the ventricular activations extracted from the EGM considering a window 250 ms long (red boxes). Bottom panel, left: EGM with the identified ventricular activations. Bottom panel, right: An example of the obtained ventricular template.

on the cross-correlation function which tests the similarity between a QRS complex template and the ECG signal. The algorithm returns the maximal correlations and the time shift related to them that corresponds to the R–wave

peaks. Templates of the of VA were obtained by extracting windows of length equal to 250 ms from the EGMs around the detected R-waves and the far-field ventricular potentials were removed by substracting the template (Figure 3.2). The implemented algorithm for the LAAT detection is a modified version of the
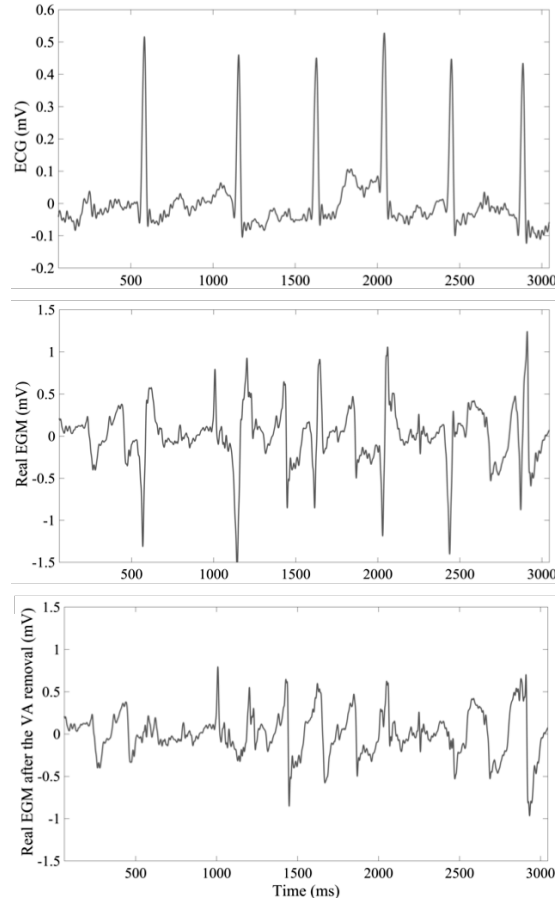
Figure 3.2: Top panel: ECG signal; middle panel: example of a EGM characterized by both AAs and VAs; bottom panel: the same EGM after the ventricular far-field removal.

electrogram recomposition from sinusoidal wavelets proposed by Kuklik et al. [92]. The method uses the phase information of the recontructed signals for the AA detection which correspondes to the position of the phase inversion (phase

transition from π to -π).

The sinusoidal reconstruction of the unipolar EGM was obtained considering a sinusoidal wavelet for each time point of the original signal on which the derivative is negative (Figure 3.3). The wavelet amplitude is proportional to the slope of the signal and its period is equal to the mean cycle length of the EGM. The mean cycle length was calculated by estimating the dominant period for each signal as the inverse of the DF. The DF was computed considering the method previously published in literature in [95]. Before estimating the power spectral density using the Welch's method, the Botteron's approach was applied for each signal [95]. This pre-processing consists in three steps: (1) band-pass filtering at 40-250 Hz, (2) absolute value, (3) low-pass filtering at 20 Hz. Since the patients are affected by paroxysmal AF, the DF value was defined as the frequency with the highest power in the range of 3-10 Hz. The recontructed signal is obtained by summing the sinusaoidal wavelets and its phase results in a "sawthooth" shape (Figure 3.3). The phase is estimated considering the AS whose imaginary component is obtained applying the HT to the signal. The AS is a complex signal whose negative components have zero amplitude.

$$AS(t) := u(t) + jH(u)(t).$$

where u(t) is the signal and H(u) is its HT. The HT is a linear operator which takes a funcion f(t) and produces a function H(f)(t) in the same domain. HT is the convolution between the Hilbert transformer and the function f(t).

$$H(u)(t) := f(t) * h_{\mathrm{H}}(t) = \frac{1}{\pi} \int_{-\infty}^{\infty} \frac{f(t)}{t - \tau} d\tau.$$

where:

$$h_{\mathrm{H}}(t) = \frac{1}{\pi t}.$$

The transfer function of HT is:

$$HT(\omega) := -jsign(\omega).$$
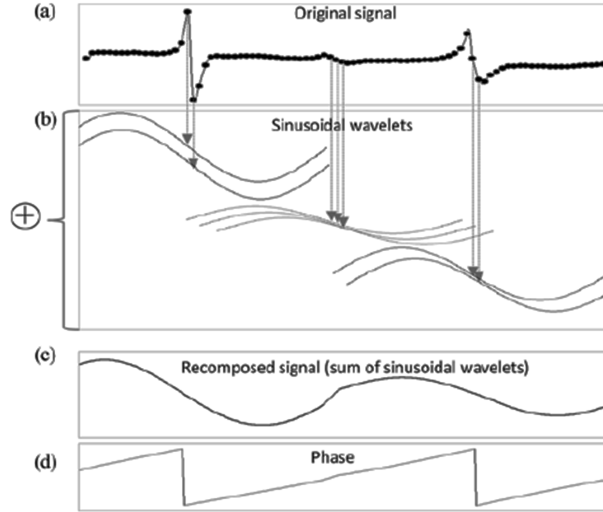
Figure 3.3: Workflow of the sinusoidal recomposition of the EGMs. a) Original signal. b) Generation of the sinusoidal wavelets in corrispondence of the all negative deflections. c) Recomposed signal obtained from the sinusaoidal wavelets. d) Phase of the recomposed signal.

where:

$$sign(\omega) = \begin{cases} 1 & \omega > 0 \\ 0 & \omega = 0 \\ -1 & \omega < 0 \end{cases}$$

HT produces a -90° degree phase shift for the positive frequency and a +90° degree shift for the negative. The amplitude do not change. The phase of the signal is obtained from the AS:

$$\phi = \arctan \frac{-f(t)}{H(f)(t)}.$$

The SR method was tested on real clinical data acquired during RFCA using the basket catheter. The obtained results were not satisfactory, especially in presence of noisy signals. In some cases, the detected phase inversion do not correspond to the real AAs (Figure 3.4). Since, a correct AA localization is
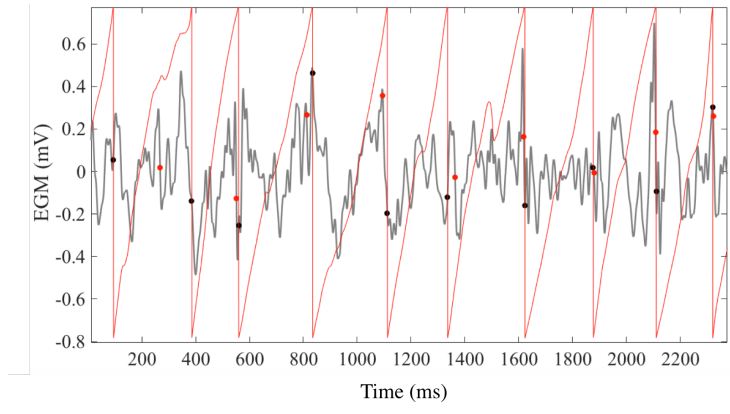
Figure 3.4: An example of the result on a portion of EGM (2400 ms) obtained applying the SR method. The red line represents the phase estimated on the reconstructed signal. The detected AAs (black dots) were compared with the manual annotations performed by the expert (red dots). In this case, five AAs were not correctly identified by the algorithm.

important for indentifying and quantifying the spatiotemporal organization of AF, a modified version of the SR method was developed in order to improve its outcome. In the proposed approach, considering a typical morphology of an atrial activation, the wavelets were only generated in correspondence of all negative derivative points that satisfy some conditions. For this purpose, additional constraints, empirically selected, for sinusoidal wavelet generation were taken into account, by adding some thresholds on the slope of negative deflections ($\leq$ -0.012 mV/ms), on their amplitude (≥ 0.034 mV) and on their duration ([50-80] ms). The HT was applied to the reconstructed signals and the resulting phase inversion points were used to center a window with the length proportional to the dominant period, in which the point with the maximum negative derivative was considered as the LAAT (Figure 3.5). This new method was named NDSR. Figure 3.6 shows the result of the application of the NDSR method on the same portion of the EGM shown in Figure 3.4.

Once the LAATs were detected, 3D phase maps were constructed on the por-
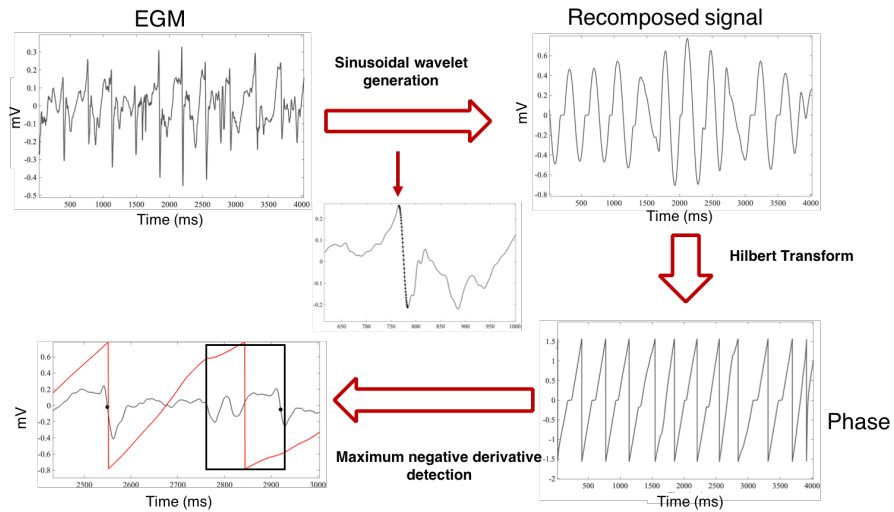
Figure 3.5: Schematic workflow of the NDSR method. The sinusoisal wavelets are generated considering the additional thresholds on negative deflections. Around the phase inversions, the maximum negative derivative point is estimated and correspondes to an LAAT.
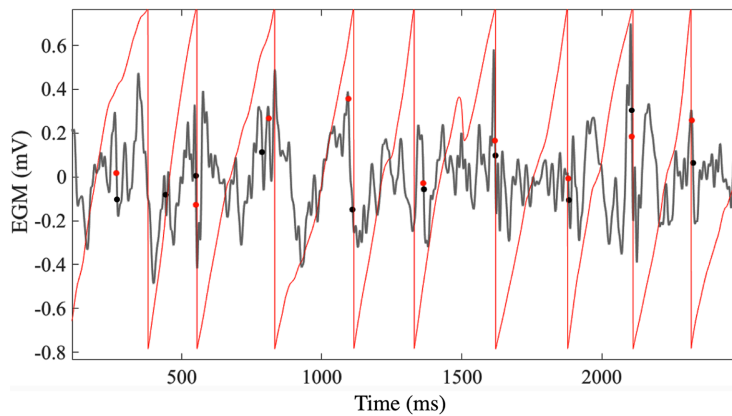
Figure 3.6: Result of the application of the NDSR method. Only two LAATs were incorrectly classified.

tion of the 3D geometry of the LA covered by the catheter. To each point on the anatomy was assigned the phase value computed considering the signal from

66

the nearest electrode (Figure 3.7)

The interpolation between nearby electrodes was not considered in our analysis. A first attempt we decided to use for the rotor localization only the original signals and not to introduce additional informations that might influence the analysis. This choice is supported by a recent study conducted by Martinez -Mateu et al. [96] demonstrated how the phase interpolation can bring to the generation of phantom PS points on the basket maps. For the validation of the
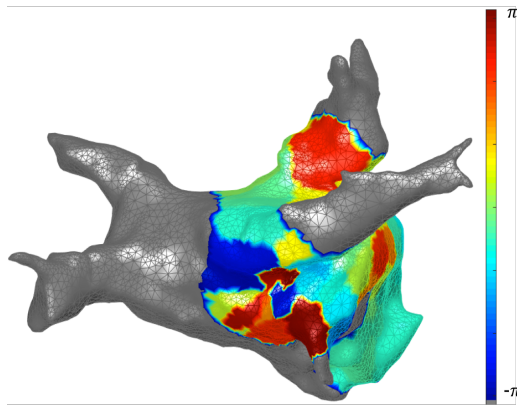
Figure 3.7: An example of 3D phase map reconstruction in one patient and in one frame. The grey regions represent the portion of the LA not covered by the catheter.

NDSR algorithm, as first attempt, the LAATs were compared with the manual ones performed by two experts. Unfortunately manual annotation of LAATs is a time-consuming and challenging process which suffers from high intra/inter-observer variability (Figure 3.8). Therefore an approach based on synthetic signals in which LAAT positions are known, was used for the proposed algorithm validation.
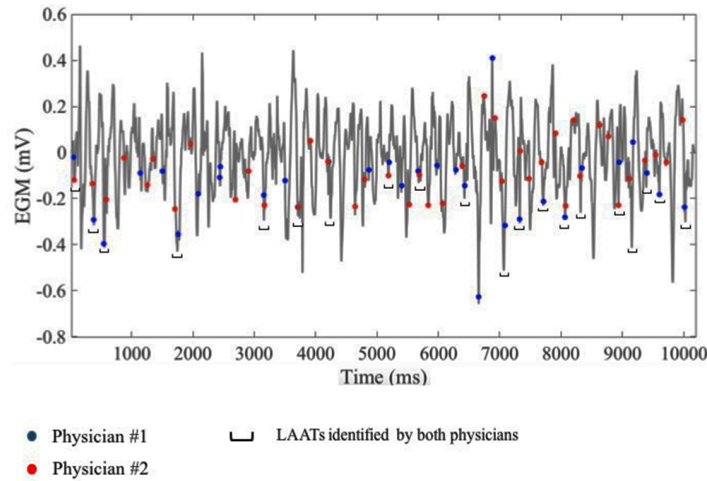
Figure 3.8: Manual annotations performed by the physicians (red and blue dots) on a real EGM without the ventricular activations. In this example, the agreement was found only for 20 LAATs.

3.3   Synthetic EGM generator

The content of this paragraph is based on the article "Towards a repository of synthetic electrograms for atrial activation detection in atrial fibrillation", by Maddalena Valinoti, Francesca Berto, Stefano Severi, and Cristiana Corsi, which was submitted to *Computer Methods and Programs in Biomedicine*. The SEGMs generated for the NDSR method validation were provided as supplementary material.

PhysioNet offers free web access to large collections of recorded physiologic signals including ECG and related open-source software. Researchers on ECG analysis take advantages of such resources to test new methodologies and share data and algorithms for data analysis. Several dynamic approaches have been proposed for modeling synthetic ECGs in heterogeneous conditions and with different PQRST-complex morphologies [97, 98]. Unfortunately, no atrial unipolar EGMs in the left atrium, not from real patients or synthetic are available in

PhysioNet and no models have been proposed for simulating realistic EGMs derived directly from the real ones.

For this purpose a new and fast workflow for the generation of realistic SEGM in AF condition with different levels of noise and at different AF rates was proposed. In addition the SEGM signals will be shared with the scientific community as a first step towards a repository of synthetic and real atrial signals supporting the evaluation of new approaches on the same database to allow direct comparison between them.

Material and Methods The SEGM generator was constructed starting from the clinical data and the manual annotations performed by the experts. A subset of 19 real EGMs characterized by different AA patterns was visually selected for the SEGM generation and an example of the selected signal after the band-pass filtering and far-field QRS complex substraction was shown in the Figure 3.9. It is well known that both atrial and ventricular activity can be recognized
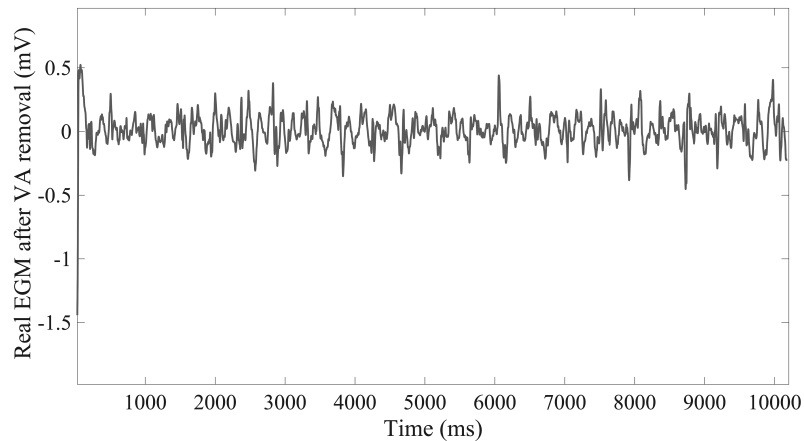
Figure 3.9: One of the 19 signals selected for the SEGM generation after the VA removal.

on a real EGM. Therefore, the SEGM was designed including these two main components (AA(t) and VA(t) respectively):

$$SEGM(t) = AA(t) + VA(t).$$

VA(t) represents a noise superimposed to the atrial signals, due to the far field effects of the ventricles especially during their depolarization phase. The atrial activity can be seen as the sum of two subcomponents:

$$AA(t) = A_{far}(t) + A_{near}(t).$$

where $A_{far}(t)$ is the far field effect that interferes on $A_{near}(t)$ that represents the LAAT, hence the actual signal of interest. The A_{far} component represents signals from far sources that result in the noisy effect usually overlapped to the near field activity. This component was modeled using an autoregressive (AR) model. The AR model is based on the hypothesis that a time series can be considered as the output of a linear filter whose input is white noise. The current sample of the process is expressed as the sum of the weighed previous values and a noise component:

$$A_{far}(t) = \sum_{k=1}^{p} c_k A_{far}(t-k) + w(t).$$

where w(t) is the white noise given in input to the model; p is the order of the model and c_k its coefficients [99, 100]. The coefficients and the variance of the white noise were estimated by applying the Yule-Walker equations based on the evaluation of the autocorrelation function. The Yule-Walker equations entail the recursive computation of the autocorrelation function r(s) of the AR process with the lag $s \succ 0$:

$$r(s) = \sum_{k=1}^{p} c_k r(s-k) + \delta(s)\sigma^2.$$

where δ(s) is a discrete impulse and σ^2 is the variance of the white noise. The coefficients c_k and the order p were derived by fitting the 19 EGMs as explained in the following. A_{far} corresponds to each segment of the real EGMs between

70

two annotated atrial depolarizations. AAs were excluded considering a 80 ms window around the maximum negative derivative of the manually annotated activations. The window length was set considering the typical morphology of an atrial activation and to ensure the activation patterns are completely excluded from the atrial far field template. Segments shorter than 150 ms were discarded. Each segment was then fitted by an AR model of order p, with p in the range [1- 40]. The optimal order p for each segment was obtained minimizing the Akaike's information criterion (AIC):

$$AIC(p) = nlog(\sigma_p^2) + 2p. \qquad\qquad \text{p=1,...,40}$$

where n is the length of the segment and $\sigma^2{}_p$ is the variance of the white noise at the order p. The optimal order p for each signal was estimated by averaging the order p for each segment and it was used to re-compute the c_k and $\sigma^2{}_p$ for each segment. For each EGM these coefficients and the variance were used to compute A_{far}. The proposed approach for A_{far} construction is depicted in Figure 3.10 (a-b). The A_{near} component was extracted from the 19 real EGMs considering the electrophysiologists' agreement on LAAT detections. Each extracted atrial template was multiplied by a cosine function in order to smooth the extremities and avoid sudden transitions at the beginning or the end of each template that may cause spurious atrial activation patterns into the SEGM. In addition, for each template, its mean value was subtracted. Figure 3.10 (c) shows an example of atrial template derived from a real EGM (Figure 3.10 (a)).

The template locations on the A_{far} signals were assigned considering that the intervals between successive activations can be described by a gamma distribution. The gamma distribution is a probability function defined by a scaling (θ) and a shaping (s) parameter that can be estimated considering the following equations:
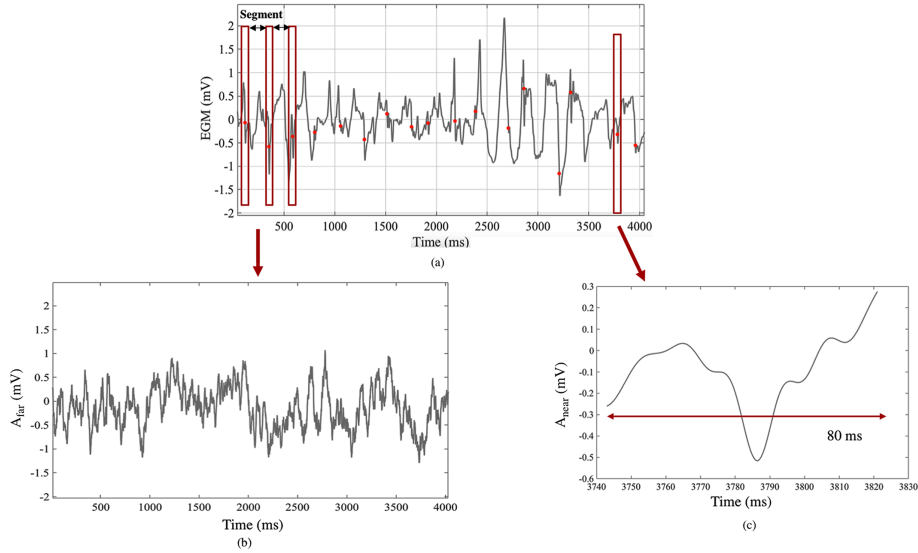
Figure 3.10: Workflow designed for the atrial component construction. (a) Example of atrial segments extracted from the real EGM and used to estimate the AR model. The AAs were excluded considering windows 80 ms long (red box) around the maximum negative derivative points of the manually annotated activations (red dots); (b) Output of the AR model that represents the A_{far} signal; (c) A_{near} component.

$$\begin{cases} s\theta = mean(IT) \\ s\theta^2 var(IT) \end{cases}$$

The mean and the variance of the atrial periods (IT) were directly derived from real EGMs and set to 250 ms and 992 ms^2 respectively; the computed parameters were: s= 62, θ=4.

The atrial templates were randomly selected and located on the A_{far} signal through the gamma distribution.

The ventricular component to be located on the synthetic signals were obtained considering the extracted windows from the real EGMs with the length equal to 250 ms around the detected R-waves. This value that may be considered

72

rather long, was set to be sure to exclude the atrial activity corresponding to the entire QRS complex.

To place the ventricular far- field potential on the SEGM composed by the A_{far} and A_{near} components, an atrio-ventricular (AV) node model was used. The model takes in input the atrial rate [101] and gives as output the instants of time in which ventricular activity starts. These instants were used to place the VA templates in the signal already composed by the A_{far} and A_{near} components. The completed workflow describing SEGM generation is shown in Figure 3.11. For each SEGM, all components (A_{far}, A_{near} and the VA) come from the same real EGM. Six sets of 50 SEGMs characterized by an increasing level of noise were generated by modifying the values of the variance of the white noise ($\sigma=a\sigma$, with a= 0, 0.1, 0.2, 0.5, 0.7, 1) used as input to the autoregressive model. An additional set of 50 SEGMs was generated considering a varying value for the variance of the white noise, a=f(A_{near}), based on the amplitude of the atrial activations of the real EGMs with the aim to reduce the variance if the amplitude is too small.

Data Analysis The realism of the synthetic EGMs was assessed by three electrophysiologists. A dataset of 50 EGM signals (25 SEGMs and 25 real EGMs) was built for this visual evaluation. The 25 SEGMs lasting 2 seconds were randomly selected from the set of 350 SEGMs generated as previously described. The experts were asked to indicate which signals were real and which not. After 2 weeks the experts repeated the analysis on a randomly selected subset of 21 signals belonging to the same set of 50 EGMs previously evaluated. This set included 10 EGMs and 11 SEGMs. Sensitivity, specificity, positive predictive value and negative predictive value were computed considering the expert indication on the 50 signals; agreement in repeating the same choice (real or synthetic signal) was also evaluated.
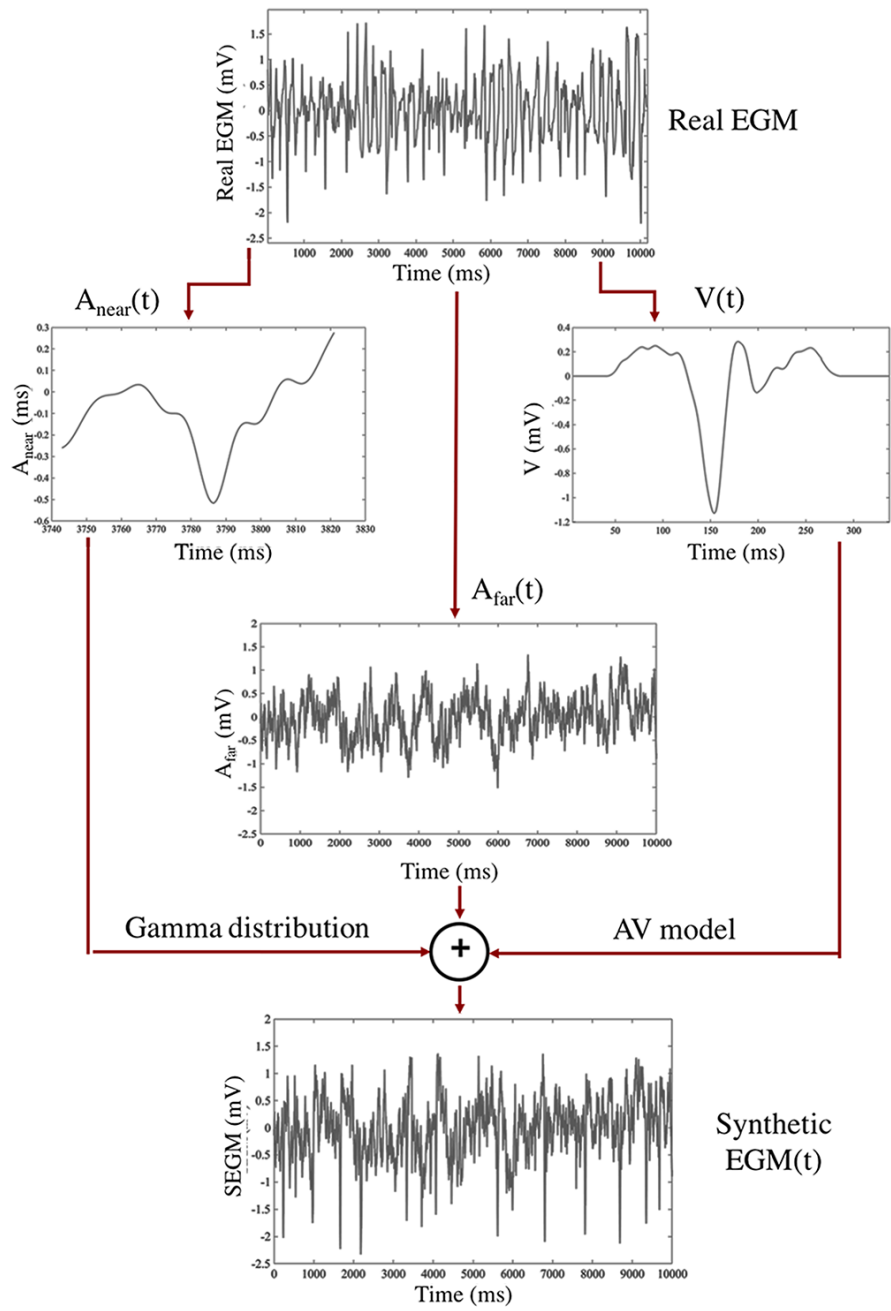
Figure 3.11: Complete workflow designed for SEGM generation.

	TP	FN	FP	TN	SE	PPV	SP	NPV
Expert1	17	8	6	19	68%	74%	76%	70%
Expert2	20	5	21	4	80%	49%	16%	45%
Expert3	7	15	15	10	28%	32%	40%	40%

Table 3.1: Results of EGM classification. TP=true positive; FN=false negative; FP=false positive; TN=true negative; SE=sensitivity; PPV=positive predictive value; SP=specificity; NPV=negative predictive value.

Results The time required to generate the synthetic EGMs was less than 1 minute once annotated EGMs are available. The sampling frequency of the generated SEGMs is 2000 Hz. An example of one real EGM (a) and three derived synthetic EGMs with different level of noise (b-d) is shown in Figure 3.12. In Table 3.1, are reported the results of the analysis performed by the three experts in judging EGMs. Expert #3 was not able to judge three EGMs and was not able to explain the reason. An example of an EGM that was correctly identified as synthetic by the three experts is reported in Figure 3.13 (top panel) together with an example of a real EGM in which the three observers were not in agreement (bottom panel). When experts repeated the analysis on the 21 signals after two weeks, expert #1 agreed with his previous annotations in 15 signals, of which 8 were annotated as real and 7 as synthetic. The 8 EGMs classified as real included 4 real EGMs and 4 SEGMS; the 7 signals recognized as SEGMs included 1 EGM and 6 SEGMs. Expert #2 agreed in recognizing the entire dataset as 19 real and 2 synthetic signals. The 19 real EGMs included 10 EGMs and 9 SEGMs; the 2 signals recognized as SEGMs included 1 EGM and 1 SEGM. Expert #3 agreed in recognizing 11 signals of which 6 were annotated as real and 5 as synthetic. The 6 real EGM included 1 EGM and 5 SEGMs; the 5 signals recognized as SEGMs included 3 EGM and 2 SEGMs.

Discussion This is the first study aimed at the generation of synthetic unipolar electrograms in AF.
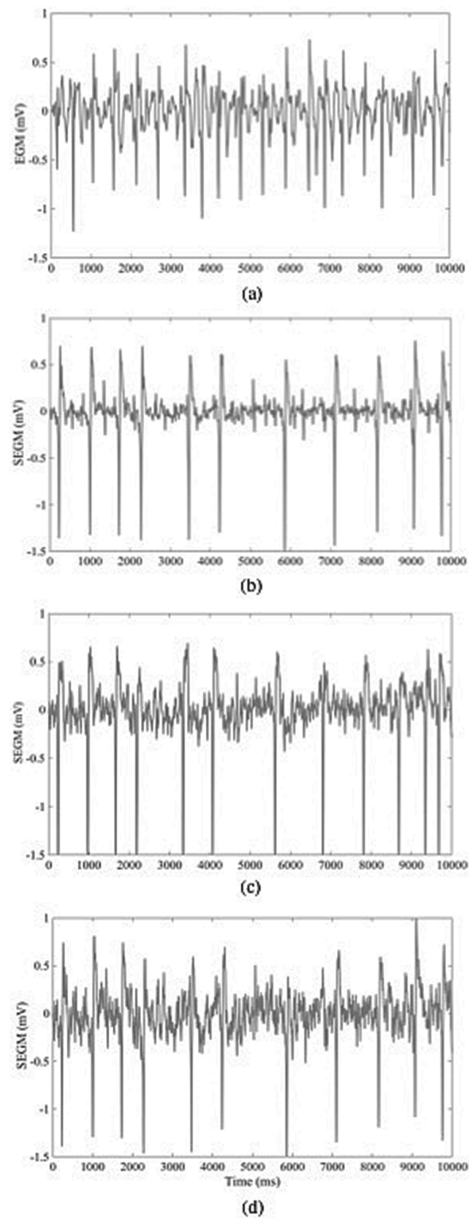
Figure 3.12: SEGMs with different levels of noise ((b) 10%, (c) 50%, (d) 100%), obtained starting from the real EGM shown in (a).
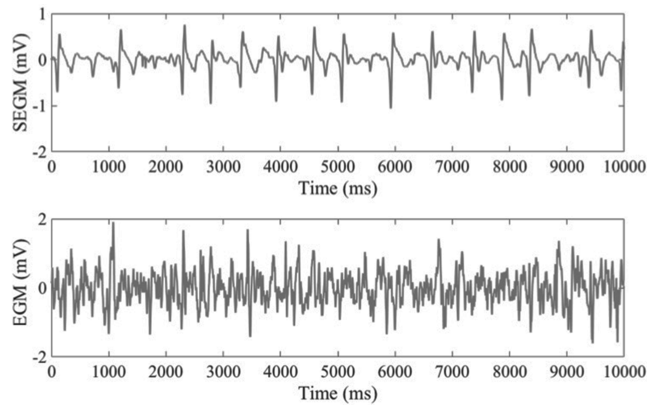
Figure 3.13: Top panel: example of a SEGM correctly identified by the three observers in each test; bottom panel: example of real EGM characterized by a high intra/inter observer variability.

EGMs were generated as the sum of two contributions due to atrial and ventricular activities, directly derived from real EGMs that have been manually annotated. Results showed the synthetic EGMs are realistic and electrophysiologists were not able to distinguish them from real EGMs.

Expert #1correctly recognized 72% of signals; this percentage decreased to 48% and 34% for expert #2 and expert #3 respectively. On the entire dataset, the three experts classified as real EGMs 46%, 82% and 44% of signals, confirming high variability between experts. In this group of "real recognized" EGMs, 26%, 51% and 68% were SEGMs for expert #1, #2 and #3 respectively. For the three experts 24%, 84% and 60% of SEGM were misclassified and considered real.

Based on the results on repeatability of annotations, two out of three electrophysiologists reported high reproducibility percentages in the two sessions (72% and 100% respectively); however, in the EGM annotations, 50% of real signals were incorrectly classified by expert #1 as false positive. Expert #2 classified 91% of EGMs real including 50% of incorrect classification for both real and synthetic signals. EGMs are characterized by a huge variability depending on the level of noise and the position of electrodes, therefore these results are not

surprising. Expert #3 seemed to perform the choises almost randomly, confirming how synthetic signals look like real signals. Overall, based on these results we can state synthetic EGMs look realistic. The only approach designed to reproduce realistic EGMs is the one proposed by Rivolta et al. [100]. In their study, both near field atrial activity and ventricular activity contributions are obtained by summing up the potentials generated by a dipole moving in a uniform infinite medium along specific directions.

The choice to directly derive these contributions from real EGMs allows us not to add potential unrealistic approximation due to the use of the dipole modeling to simulate the propagation complex signals. Differently from their algorithm we focused on the AF condition and we generated signals representative of different levels of noise as it happens in real conditions in different patients.

The developed workflow is effective and could be easily adopted to generate SEGMs in different arrhythmic conditions (persistent AF, atrial flutter, ..) starting from real EGMs and allowing to reproduce their inter-subject variability, for example, in morphological aspects of atrial activations, also including fractionated EGMs. Moreover, for each considered pathological condition, model parameters may be tuned to describe different atrial and ventricular rates and far field noise. In the present study real EGMs from patients with paroxysmal AF were analyzed but the same approach might be applied to other arrhythmic conditions. Obviously this statement should be proved but no theoretical constraints limit the application of our approach to EGMs of patients affected by different kind of AF.

In addition, the proposed workflow could be further simplified for the ventricular activity step since a realistic sequence of RR intervals obtained from real signals could be used to locate the ventricular far-field instead of using the AV node model.

The model is stationary respect to the near field and atrial activation frequency but this work wants to provide a dataset to facilitate the comparison of different signal processing techniques. Similar approaches have been proposed in recent years for different bio-signals in the mono- bi- and three-dimensional domain,

including ECG [98], echocardiographic data [102], EMG [103].

Using such synthetic signals, the performance of a given technique, can be presented and such performance assessment could be used as a "standard" and would enable clinicians to ascertain which biomedical signal processing techniques is the best for a given application. In the field of AF the availability of "standard" synthetic EGMs is particularly crucial. Indeed, variability in atrial activation detection in real EGMs is huge.

The manual annotation of LAATs by two electrophysiologists resulted in a very poor agreement. In nineteen EGMs of 10 s duration each, The manual annotations resulted in the detection of 443 LAATs from physician #1 and 534 LAATs from physician #2. Only 177 LAATs were detected by both observers considering a windows of 80 ms. Consequently, differently from other fields in which manual detection is considered the gold standard, for this specific analysis it results unreliable.

The seven sets of 50 SEGMs we generated using the described approach will be available for the scientific community. Seven .mat files were provided together with the "true" LAATs and the R-wave peak locations.

Since nowadays, a large research effort is devoted to better understanding the mechanisms underlying AF and a correct LAAT detection is crucial for AF drivers localization, this study contributes to standardize the validation of the numerous approaches designed and tested for AF driver detection.

3.3.1   Validation of the NDSR method on SEGMs

The NDSR method was tested on SEGMs and the detected LAATs were compared with the ground truth atrial activations (A_{near}). The first set of SEGMs was excluded from the validation analysis since it is characterized by zero level of noise and does not represent a real condition. The results of the validation are shown in the Table 3.2. A detection was considered successful if it matched the A_{near} within a window of 50 ms.

As expected, the results of the validation showed that the performance of the

#	TA	EA	TP	FP	FN	PPV (%)	Se (%)
1	2049	2054	1892	162	157	92	92
2	2048	2000	1832	168	216	92	89
3	2000	2058	1765	293	235	86	88
4	2049	2128	1629	499	421	77	79
5	2000	2084	1399	685	605	67	70
6	2000	2110	1254	852	742	60	63

Table 3.2: Quantitative results of LAAT detection on synthetic EGMs for increasing levels of noise. TA: true activations; EA: estimated activations; TP= true positive; FP/FN=false positive/negative; PPV= positive predictive value; Se=sensitivity.

algorithm on LAAT detection on SEGMs is high when the level of the noise is low. Nervethless, the performance of the algorithm remains accurate also in presence of a high level of the noise.

The SR method was also tested on the same dataset composed by 350 SEGMs in order to compare the performances of the two methods. The results of the SR application of the SEGMs are shown in Table 3.3. The two techniques reported similar value of PPV and Se for low levels of noise, up to k=0.2 the PPV and sensitivity of the SR method were systematically lower up to 10%.

3.4 Rotor detection algorithm

The rotor detection algorithm is based on the search of the PS points. PS is a point surrounded by a gradual phase transition between neighbouring points up to an inversion phase (from π to -π). The classical approach using for PS detection is based on closed path integral of the phase gradient:

$$\oint_c \nabla \varphi d \overrightarrow{l}.$$

80

#	TA	EA	TP	FP	FN	PPV (%)	Se (%)
1	2049	2116	1864	252	185	88	91
2	2048	2075	1892	156	183	92	91
3	2000	2074	1674	400	326	81	84
4	2049	2171	1522	649	528	70	74
5	2000	2147	1242	905	759	58	62
6	2000	2192	1096	1096	904	50	55

Table 3.3: Quantitative results of LAAT detection on synthetic EGMs obtained with SR method. TA: true activations; EA: estimated activations; TP= true positive; FP/FN=false positive/negative; PPV= positive predictive value; Se=sensitivity.

where c is a closed loop surrounding the given point, φ is the phase value in space, ∇ is a spatial derivative. PS is detected if, taking the consecutive phase differences between neighboring points moving along the path c, there is only one large phase difference corresponding to the transition to a new cycle.

In case of a discrete mesh of electrodes such as the Constellation catheter, the integral has to be discretized and approximated. The loop c becomes a ring of electrodes encircling a point that could be a PS point [104]. An example of 2x2 ring of electrodes and a PS point on 2D spatial domain are shown in the Figure 3.14. The implemented algorithm is able to detect PS points in 3D domain. To each region of the LA mesh, the neighboring ones were estimated and the phase gradient between them was computed ($\nabla\phi$). If the region under investigation is surrounded by a gradual phase transition between its neighboring regions plus an inversion phase, the mean point of their centroids represents a PS point.

Since, for each time frame, the algorithm might detect several PS points due to the discretization and the catheter resolution, a PS point was defined as the pivot of a rotor if its lifespan is greater than one AF cycle (Figure 3.15). In addition, the rotor was defined stable in the space if the coordinates of its pivot
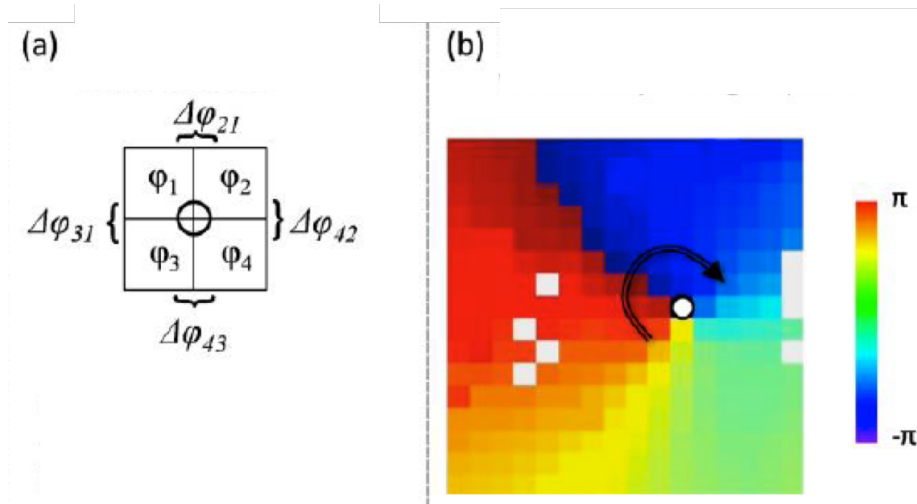
Figure 3.14: (a) PS detection using 2x2 ring of electrodes. (b) 2D phase map of large rotating wave with its PS point (white dot).

(or PS point), remains inside a region of radius equal to 0.5 cm throughout its lifecycle. Otherwise, the rotor was defined meandering. For each detected stable
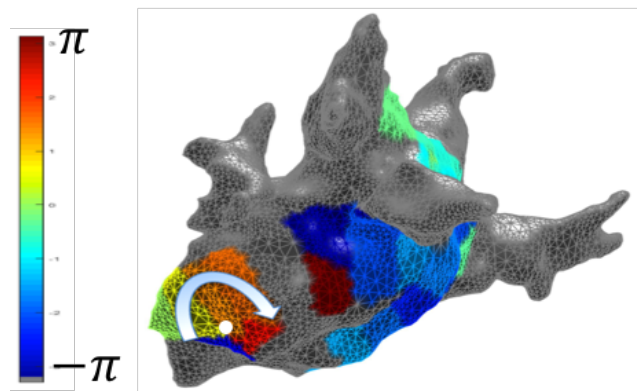
Figure 3.15: Phase map reconstructed in one patient and in one time frame. The map was obtained as described at page 65. The white arrow indicates one detected stable rotor and the white dot represents its pivot. In this example the AF cycle is 250 ms.

or meandering rotor, its persistance in time was also calculated considering the threshold 0.5 cm on the maximum distance between the coordinates of its phase singularity points estimated frame by frame.

The rotor detection algorithm was validated using an atrial computational model and preliminary results are shown in the following section. This part of the project was developed in collaboration with the Karlshrue Institute Technology (KIT) in Karlshrue, Germany and received the funding from MIUR-DAAD Joint Mobility Program, 2016-2017.

3.4.1 Validation of the rotor detection algorithm

A computational model of LA electrophysiology was used as benchmark for the rotor detection algorithm validation. The 3D LA anatomy was derived from the pre-operative MRA data using the new segmentation method of the LA described in the Chapter 2. The atrial anatomy was converted into a cubic lattice for the simulation. Atrial activation was simulated on the 3D anatomy using the monodomain approach [105] and a variant of the Courtemanche et al. action potential model, accounting for spatial heterogeneity and AF related ionic remodeling [106]. Sinus activation was simulated by pacing the model at the insertion point of the Bachmann bundle and at the Fossa Ovalis with a physiological delay of 26 ms. Reentry was initiated by placing an extra stimulus in a circular area of tissue of radius 10 mm. One meandering rotor was generated on the posterior wall (Figure 3.16 (a)) and the simulation was 2s long. Sinus activation was applied once and then suspended. EGMs were simulated by using the assumption of an infinite homogeneous medium[107]:

$$\Phi(P,t) \propto \int_{Vol} \frac{I(Q,t)}{||P-Q||} dQ.$$

where ϕ is the electric potential, P the sensing position and I the transmembrane current at each position Q within the myocardium. Sampling frequency was 1000 Hz.

83
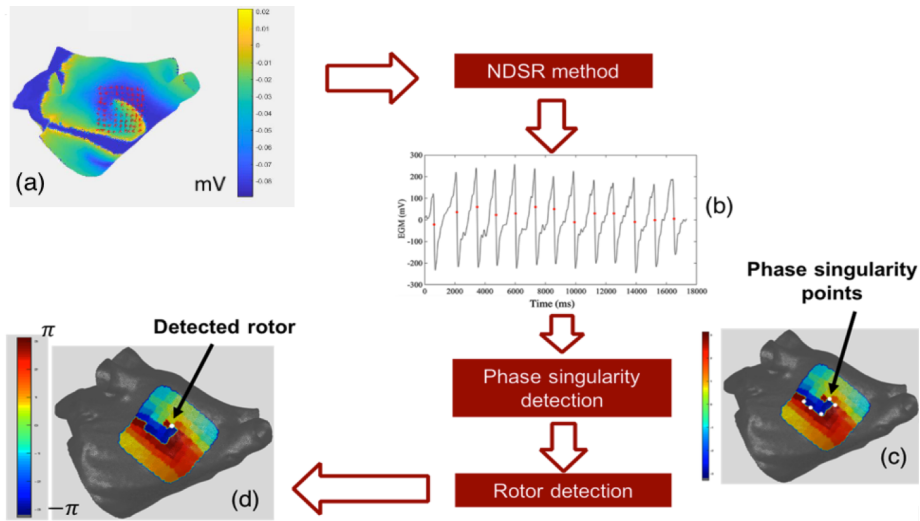
Figure 3.16: Schematic workflow of the rotor detection applied on the simulated data.

For the validation, a 2D grid in contact to the atrial wall, composed by 9x9 electrodes with 3 mm as intra-electrode spacing was generated (Figure 3.16 (a)) . On the simulated atrial EGMs the processing described so far was applied. The simulated AF frequency was 7.8 Hz. The signals were band-pass filtered (3-80 Hz) and then the NDSR algorithm was used for the LAAT detection (Figure 3.16 (b)). The 3D phase map was reconstructed and the PS points were detected (Figure 3.16 (c)). The simulated rotor was correctly identified considering the PS with lifespan greater than 128 ms (Figure 3.16 (d)). As highlighted in Figure 3.17, the detected pivot is close to the real one. In addition the trajectory of the pivot of the rotor detected with the algorithm was compared with the simulated one and the result is shown in the Figure 3.18. The trajectory of the simulated rotor was manually traced. The centroids of the trajectories were estimated and the distance between them was computed and was 3.6 mm. The trajectory of the detected pivot is influenced by what we called the "border artifacts" of the grid. The LA surface is divided in regions, each one associated to the EGM acquired by the closest electrode. The regions closer to the grid

84

boundary are bigger since they are not shared between neighbouring electrodes. When we compute the PS pivot coordinates, these regions weight more than the smaller ones and therefore the trajectory of the pivot results enlarged towards this regions as shown in Figure 3.18. Preliminary comparison with the rotat-
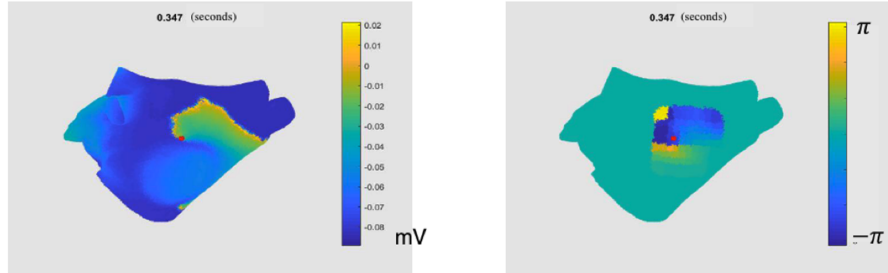
Figure 3.17: Action potential map of the simulated rotor (left) and the phase map reconstruction (right) in the same frame. The red dot in the both figures represents the coordinates of the pivot detected by the algorithm.
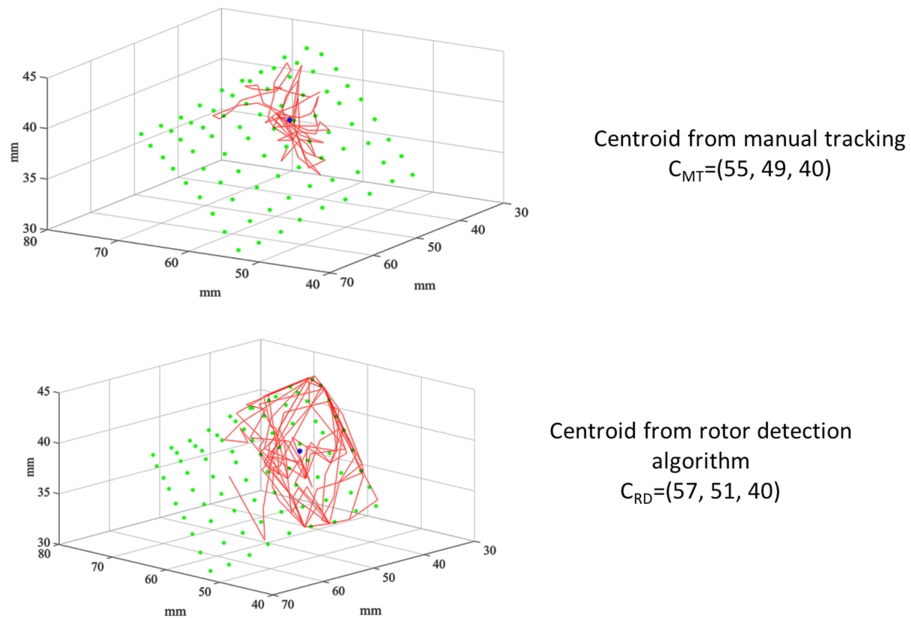
Figure 3.18: top panel) Trajectory of the real pivot of the rotor. bottom panel) Trajectory of the detected pivot.

ing waves generated by the computational model showed correct identification of the PS point. The distance between the centroids of the "real" pivot and of the detected one is negligible respect to the typical size of an ablation (<1 cm^2) and therefore the rotor detection algorithm seems to be able to provide a correct information about the region to ablate for the rotor activity block.

We performed additional tests including more than one rotors, not necessarily centered in the grid. Results showed the estimate is reliable only for rotors well centered with the catheter and therefore a complete coverage of the rotor is ncecessary for its identification.

In addition, in order to study the effect of the distance to the atrial wall, a set of "toy" catheteters were generated and placed at different distances from the wall (0.5 cm, 1 cm, 1.5 cm) (Figure 3.19) As intuitively expected, an increase in
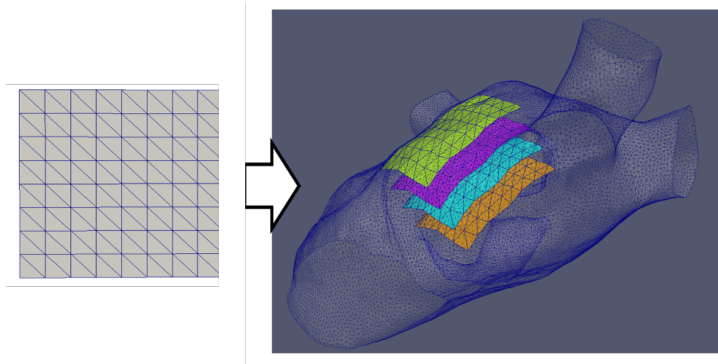
Figure 3.19: Grid catheter placement. The grid is first computed in a 2D coordinate system and then adapted to the 3D atrial geometry. The different colors represent grids at different distance from the wall: green (contact); magenta (0.5 cm); cyan (1cm); orange (1.5 cm).

distance implies an increased sensitivity to "far-field" effects (i.e. coming from regions other than the mapped one). Results in rotor identification was correct up to 0.5 cm with a distance between the centroids equal to 1.2 mm; at 1 cm, the algorithm was not able to detect the rotor for all its lifespan (2s). A wall distance of 1.5 cm is obviously too large for a reliable phase computation and

with this setting the algorithm was not able to detect the simulated rotor.

The developed technique may provide a tool for investigating the effects of different catheter coverage, and of the intra-spline distance on the rotor detection.

3.5 Analysis of the influence of the catheter coverage on the rotor localization

As mentioned in the Chapter 1, considering the basket's size more used in clinical practice, the covered area by the Constellation catheter is wide and is about 117 cm^2. For the evaluation of the catheter coverage on the rotor detection, the implemented workflow was applied on EGMs acquired by the PentaRay catheter (Biosense Webstern, CA, USA) in five paroxysmal AF ablation procedures. The PentaRay is composed by 20 electrodes located in five splines and its coverage is 7 cm^2 (Figure 3.20). The two steps of the workflow implemented for
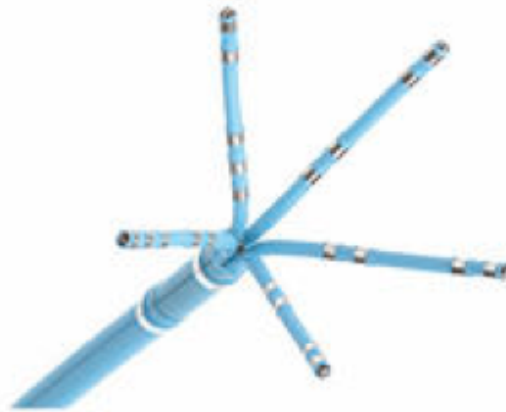
Figure 3.20: PentaRay catheter.

the LAAT and rotor localization were tested on PentaRay data. An example of the obtained result is shown in the Figure 3.21. The results on the rotor
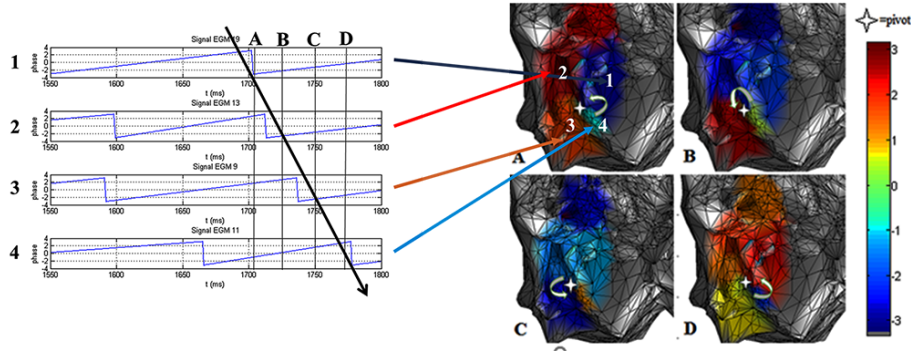
Figure 3.21: Example of phase maps (right) in four different frames obtained from the EGMs acquired by the PentaRay catheter. The white arrow indicates the detected rotor for each frame based on the phase information of the signals (left).

detection obtained by the two catheters on the clinical data were compared (Figure 3.22). Considering 13 mm as maximum distance between the electrodes
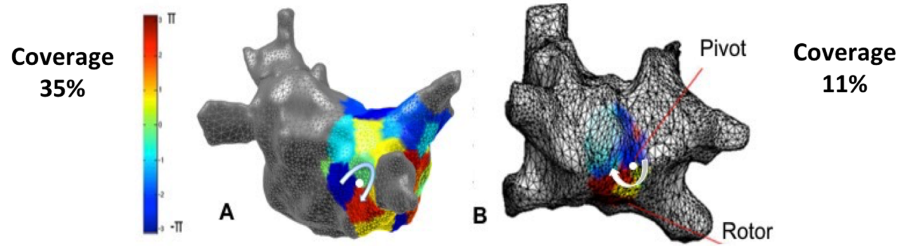
Figure 3.22: LA geometry with the catheter coverages (coloured regions, A) 35.0%, B) 11.0%) and one detected stable rotor (white arrow).

and the atrial wall, the computed coverage of the basket and PentaRay catheter was: $43.3\pm7.8\%$ and $12.3\pm2.4\%$, respectively. The dominant frequency estimated and used for the sinusoidal recomposition method was 4.0 ± 0.3 Hz for the Constellation acquisitions and 4.2 ± 0.2 Hz for the PentaRay ones. The

number of stable and meandering rotors per subject detected with the basket catheter was 4.0±3.4 and 4.6±5.0, with a persistence in time of 303.2±58.2 ms and 302.3±52.0 ms, respectively. The PentaRay catheter identified 3.7±4.4 stable rotors with a persistence in time 326.0±215.2 ms and no meandering ones. Preliminary results showed the presence of stable and meandering rotors in the LA, characterized by a very short persistence in time. LA chamber coverage has a central role for meandering rotor detection and the effects of the number of the electrodes and their spacing are major challenges during AF mapping for rotor detection.

Chapter 4

Concluding remarks and future developments

In this doctoral thesis, new approaches for the structural and electrical characterization of the LA we presented, with the aim to support the investigation of the maintaining mechanisms underlying AF.

In Chapter 2, a unified and fast workflow for 3D patient-specific LA models computation (with and without PVs) was presented. The implemented models might be useful to support patient selection for RFCA and provide a reliable guidance during the therapy. The implemented approach based on a new segmentation method of the LA, proved to be effective and provides a reliable 3D LA models and an accurate LA volume estimation.

In additon, a fully automated approach for LA fibrosis quantification was designed and developed. In particular a 3D LA fibrosis patient-specific model was constructed and fibrosis quantification methods were implemented. The workflow was tested in ten patients which were classified in four stages according to the Utah classification. The obtained results demonstrated that the classification is influenced by the method applied for fibrosis assessment and a unique

and reproducible threshold to define the fibrotic regions is still lacking probably due to absence of a standardized LGE-MRI acquisition protocol.

In Chapter 3, a new approach for meandering and stable rotor localization and detection on the 3D LA surface is illustrated. This is the first study which aim to detect stable and meandering rotor in 3D domain. The workflow consisted in two steps: 1) LAAT indentification and phase map construction, 2) PS point estimation and rotor detection.

For the LAAT recognition, we designed an improved version of the SR method. This new approach was validated using SEGMs with different level of the noise. As expected, the results of the validation showed that performance of the new method is high when the level of the noise is low. However, the performance of the new algorithm remains accurate also in presence of a high level of the noise. The SR method was tested on the same dataset of the SEGMs and the performance of the mehod were systematically lower than the NDSR up to 10%. To generate SEGMs with different levels of the noise and rates in AF, a new workflow based on the real EGMs was proposed. The realism of the synthetic EGMs was assessed by three electrophysiologists. Results showed the synthetic EGMs are realistic and electrophysiologists were not able to distinguish them from real EGMs.

The rotor detection algorithm was validated using an atrial computational model and preliminary comparison with the simulated rotating waves showed correct identification of the PS point. The proposed algorithm is able to provide a correct information about the region to ablate for the rotating pattern block. In addition, the influence of the spatial coverage on the rotor localization was investigated comparing the results obtained with the PentaRay and the Constellation catheters in clinical settings. Preliminary results showed the importance of the spatial coverage of the LA for the meandering rotor localization. The identified rotors by both catheters were characterized by a very short persistence in time. Future developments of this project include the investigation of the relationship between the LA enlargement and AF recurrence and testing the implemented approach for the fibrosis assessment on a larger population.

Acquisitions of more data using both PentaRay and Constellation are required in order to better investigate the importance of the catheter coverage and the intra-electrode spacing on rotor localization.

The integration of the new approaches developed in this work for structural and electrical characterization of AF is part of the research in the near future, to investigate the role of rotors and spatial relationship between them and atrial fibrosis.

List of Figures

95

List of Tables

Bibliography

[1] Yoko Miyasaka, Marion E Barnes, Bernard J Gersh, Stephen S Cha, Kent R Bailey, Walter P Abhayaratna, James B Seward, and Teresa SM Tsang. Secular trends in incidence of atrial fibrillation in olmsted county, minnesota, 1980 to 2000, and implications on the projections for future prevalence. *Circulation*, 114(2):119–125, 2006.

[2] Paulus Kirchhof, Stefano Benussi, Dipak Kotecha, Anders Ahlsson, Dan Atar, Barbara Casadei, Manuel Castella, Hans-Christoph Diener, Hein Heidbuchel, Jeroen Hendriks, et al. 2016 esc guidelines for the management of atrial fibrillation developed in collaboration with eacts. *EP Europace*, 18(11):1609–1678, 2016.

[3] Sumeet S Chugh, Rasmus Havmoeller, Kumar Narayanan, David Singh, Michiel Rienstra, Emelia J Benjamin, Richard F Gillum, Young-Hoon Kim, John H McAnulty, Zhi-Jie Zheng, et al. Worldwide epidemiology of atrial fibrillation: a global burden of disease 2010 study. *Circulation*, pages CIRCULATIONAHA–113, 2013.

[4] Susan Colilla, Ann Crow, William Petkun, Daniel E Singer, Teresa Simon, and Xianchen Liu. Estimates of current and future incidence and prevalence of atrial fibrillation in the us adult population. *The American journal of cardiology*, 112(8):1142–1147, 2013.

[5] Lin Y Chen and Win-Kuang Shen. Epidemiology of atrial fibrillation: a current perspective. *Heart Rhythm*, 4(3):S1–S6, 2007.

[6] Curt D Furberg, Bruce M Psaty, Teri A Manolio, Julius M Gardin, Vivienne E Smith, Pentti M Rautaharju, CHS Collaborative Research Group, et al. Prevalence of atrial fibrillation in elderly subjects (the cardiovascular health study). *The American journal of cardiology*, 74(3):236–241, 1994.

[7] Bouwe P Krijthe, Anton Kunst, Emelia J Benjamin, Gregory YH Lip, Oscar H Franco, Albert Hofman, Jacqueline CM Witteman, Bruno H Stricker, and Jan Heeringa. Projections on the number of individuals with atrial fibrillation in the european union, from 2000 to 2060. *European heart journal*, 34(35):2746–2751, 2013.

[8] Massimo Zoni-Berisso, Fabrizio Lercari, Tiziana Carazza, and Stefano Domenicucci. Epidemiology of atrial fibrillation: European perspective. *Clinical epidemiology*, 6:213, 2014.

[9] Michael H Kim, Stephen S Johnston, Bong-Chul Chu, Mehul R Dalal, and Kathy L Schulman. Estimation of total incremental health care costs in patients with atrial fibrillation in the united states. *Circulation: Cardiovascular Quality and Outcomes*, 4(3):313–320, 2011.

[10] Alan S Go, Elaine M Hylek, Kathleen A Phillips, YuChiao Chang, Lori E Henault, Joe V Selby, and Daniel E Singer. Prevalence of diagnosed atrial fibrillation in adults: national implications for rhythm management and stroke prevention: the anticoagulation and risk factors in atrial fibrillation (atria) study. *JAMA*, 285(18):2370–2375, 2001.

[11] Walter P Wodchis, R Sacha Bhatia, Kori Leblanc, Nazanin Meshkat, and Dante Morra. A review of the cost of atrial fibrillation. *Value in Health*, 15(2):240–248, 2012.

[12] Simon Stewart. Epidemiology and economic impact of atrial fibrillation. *Journal of Cardiovascular Nursing*, 19(2):94–102, 2004.

[13] Guijing Wang, Mike Pratt, Caroline A Macera, Zhi-Jie Zheng, and Gregory Heath. Physical activity, cardiovascular disease, and medical expenditures in us adults. *Annals of Behavioral Medicine*, 28(2):88–94, 2004.

[14] Johan E.P. Waktare. Atrial fibrillation. *Circulation*, 106(1):14–16, 2002.

[15] Valentin Fuster, Lars E Rydén, David S Cannom, Harry J Crijns, Anne B Curtis, Kenneth A Ellenbogen, Jonathan L Halperin, Jean-Yves Le Heuzey, G Neal Kay, James E Lowe, et al. Acc/aha/esc 2006 guidelines for the management of patients with atrial fibrillation. *Circulation*, 114(7):e257–e354, 2006.

[16] Samuel Lévy. Classification system of atrial fibrillation. *Current opinion in cardiology*, 15(1):54–57, 2000.

[17] EM Vaughan Williams. A classification of antiarrhythmic actions reassessed after a decade of new drugs. *The Journal of Clinical Pharmacology*, 24(4):129–147, 1984.

[18] Ole-Gunnar Anfinsen. Non-pharmacological treatment of atrial fibrillation. *Indian pacing and electrophysiology journal*, 2(1):4, 2002.

[19] Rick A Nishimura, Catherine M Otto, Robert O Bonow, Blase A Carabello, John P Erwin, Lee A Fleisher, Hani Jneid, Michael J Mack, Christopher J McLeod, Patrick T O'gara, et al. 2017 AHA/ACC focused update of the 2014 AHA/ACC guideline for the management of patients with valvular heart disease: a report of the american college of cardiology/american heart association task force on clinical practice guidelines. *Circulation*, 135(25):e1159–e1195, 2017.

[20] Simon C Sporton, Mark J Earley, Anthony W Nathan, and Richard J Schilling. Electroanatomic versus fluoroscopic mapping for catheter ab-

lation procedures. *Journal of cardiovascular electrophysiology*, 15(3):310–315, 2004.

[21] Heidi Luise Estner, Isabel Deisenhofer, Armin Luik, Gjin Ndrepepa, Christian von Bary, Bernhard Zrenner, and Claus Schmitt. Electrical isolation of pulmonary veins in patients with atrial fibrillation: reduction of fluoroscopy exposure and procedure duration by the use of a non-fluoroscopic navigation system (navx®). *Europace*, 8(8):583–587, 2006.

[22] Martin Martinek, HANS-JOACHIM NESSER, Josef Aichinger, Gernot Boehm, and Helmut Purerfellner. Impact of integration of multislice computed tomography imaging into three-dimensional electroanatomic mapping on clinical outcomes, safety, and efficacy using radiofrequency ablation for atrial fibrillation. *Pacing and Clinical Electrophysiology*, 30(10):1215–1223, 2007.

[23] Peter M Kistler, Kim Rajappan, Stuart Harris, Mark J Earley, Laura Richmond, Simon C Sporton, and Richard J Schilling. The impact of image integration on catheter ablation of atrial fibrillation using electroanatomic mapping: a prospective randomized study. *European heart journal*, 29(24):3029–3036, 2008.

[24] Emanuele Bertaglia, Paolo Della Bella, Claudio Tondo, Alessandro Proclemer, Nicola Bottoni, Roberto De Ponti, Maurizio Landolina, Maria Grazia Bongiorni, Leonardo Corò, Giuseppe Stabile, et al. Image integration increases efficacy of paroxysmal atrial fibrillation catheter ablation: results from the cartomerge™ italian registry. *Europace*, 11(8):1004–1010, 2009.

[25] Michel Haissaguerre, Pierre Jaïs, Dipen C Shah, Atsushi Takahashi, Mélèze Hocini, Gilles Quiniou, Stéphane Garrigue, Alain Le Mouroux, Philippe Le Métayer, and Jacques Clémenty. Spontaneous initiation of atrial fibrillation by ectopic beats originating in the pulmonary veins. *New England Journal of Medicine*, 339(10):659–666, 1998.

[26] Laurent M Haegeli and Hugh Calkins. Catheter ablation of atrial fibrillation: an update. *European heart journal*, 35(36):2454–2459, 2014.

[27] Hugh Calkins, Josep Brugada, Douglas L Packer, Riccardo Cappato, Shih-Ann Chen, Harry JG Crijns, Ralph J Damiano Jr, D Wyn Davies, David E Haines, Michel Haissaguerre, et al. HRS/EHRA/ECAS expert consensus statement on catheter and surgical ablation of atrial fibrillation: Recommendations for personnel, policy, procedures and follow-up: A report of the heart rhythm society (HRS) task force on catheter and surgical ablation of atrial fibrillation developed in partnership with the european heart rhythm association (EHRA) and the european cardiac arrhythmia society (ECAS); in collaboration with the american college of cardiology (ACC), american heart association (AHA), and the society of thoracic surgeons (STS). endorsed and approved by the governing bodies of the american college of cardiology, the american heart association, the european cardiac arrhythmia society, the european heart rhythm association, the society of thoracic surgeons, and the heart rhythm society. *Europace*, 9(6):335–379, 2007.

[28] Z Khoueiry, J-P Albenque, R Providencia, S Combes, N Combes, F Jourda, PA Sousa, C Cardin, J-L Pasquie, TT Cung, et al. Outcomes after cryoablation vs. radiofrequency in patients with paroxysmal atrial fibrillation: impact of pulmonary veins anatomy. *EP Europace*, 18(9):1343–1351, 2016.

[29] Nikolaos Dagres, Maria Grazia Bongiorni, Torben Bjerregaard Larsen, Antonio Hernandez-Madrid, Laurent Pison, Carina Blomström-Lundqvist, European Heart Rhythm Association Conducted by the Scientific Initiatives Committee, Maria Grazia Bongiorni, Jian Chen, Nikolaos Dagres, et al. Current ablation techniques for persistent atrial fibrillation: results of the european heart rhythm association survey. *EP Europace*, 17(10):1596–1600, 2015.

[30] Anand N Ganesan, Nicholas J Shipp, Anthony G Brooks, Pawel Kuklik, Dennis H Lau, Han S Lim, Thomas Sullivan, Kurt C Roberts-Thomson, and Prashanthan Sanders. Long-term outcomes of catheter ablation of atrial fibrillation: a systematic review and meta-analysis. *Journal of the American Heart Association*, 2(2):e004549, 2013.

[31] Trine Krogh-Madsen, Geoffrey W Abbott, and David J Christini. Effects of electrical and structural remodeling on atrial fibrillation maintenance: a simulation study. *PLoS computational biology*, 8(2):e1002390, 2012.

[32] Yasushi Akutsu, Kaoru Tanno, and Youichi Kobayashi. The role of atrial structural remodeling in atrial fibrillation ablation: An imaging point of view for predicting recurrence. *Journal of Atrial Fibrillation*, 5(2), 2012.

[33] Jianhui Zhuang, Yi Wang, Kai Tang, Xiankai Li, Wenhui Peng, Chun Liang, and Yawei Xu. Association between left atrial size and atrial fibrillation recurrence after single circumferential pulmonary vein isolation: a systematic review and meta-analysis of observational studies. *Europace*, 14(5):638–645, 2011.

[34] Michele Miragoli and Alexey V Glukhov. Atrial fibrillation and fibrosis: beyond the cardiomyocyte centric view. *BioMed research international*, 2015, 2015.

[35] P Kohl, AG Kamkin, IS Kiseleva, and D Noble. Mechanosensitive fibroblasts in the sino-atrial node region of rat heart: interaction with cardiomyocytes and possible role. *Experimental physiology*, 79(6):943–956, 1994.

[36] Giedrius Gaudesius, Michele Miragoli, Stuart P Thomas, and Stephan Rohr. Coupling of cardiac electrical activity over extended distances by fibroblasts of cardiac origin. *Circulation research*, 93(5):421–428, 2003.

[37] Sanne De Jong, Toon AB van Veen, Harold VM van Rijen, and Jacques MT de Bakker. Fibrosis and cardiac arrhythmias. *Journal of*

cardiovascular pharmacology, 57(6):630–638, 2011.

[38] Pyotr G Platonov. Atrial fibrosis: an obligatory component of arrhythmia mechanisms in atrial fibrillation? *Journal of Geriatric Cardiology: JGC*, 14(3):174, 2017.

[39] Derek J Dosdall, Ravi Ranjan, Koji Higuchi, Eugene Kholmovski, Nathan Angel, Li Li, Rob MacLeod, Layne Norlund, Aaron Olsen, Christopher J Davies, et al. Chronic atrial fibrillation causes left ventricular dysfunction in dogs but not goats: experience with dogs, goats, and pigs. *American Journal of Physiology-Heart and Circulatory Physiology*, 305(5):H725–H731, 2013.

[40] Giulia Pontecorboli, Rosa M Figueras i Ventura, Alicia Carlosena, Eva Benito, Susanna Prat-Gonzales, Luigi Padeletti, and Lluís Mont. Use of delayed-enhancement magnetic resonance imaging for fibrosis detection in the atria: a review. *Europace*, page euw053, 2016.

[41] Eva M Benito, Alicia Carlosena-Remirez, Eduard Guasch, Susana Prat-González, Rosario J Perea, Rosa Figueras, Roger Borràs, David Andreu, Elena Arbelo, J Maria Tolosana, et al. Left atrial fibrosis quantification by late gadolinium-enhanced magnetic resonance: a new method to standardize the thresholds for reproducibility. *EP Europace*, page euw219, 2016.

[42] Felipe Bisbal, Esther Guiu, Pilar Cabanas-Grandío, Antonio Berruezo, Susana Prat-Gonzalez, Bárbara Vidal, Cesar Garrido, David Andreu, Juan Fernandez-Armenta, Jose María Tolosana, et al. Cmr-guided approach to localize and ablate gaps in repeat af ablation procedure. *JACC: Cardiovascular Imaging*, 7(7):653–663, 2014.

[43] Nassir F Marrouche, David Wilber, Gerhard Hindricks, Pierre Jais, Nazem Akoum, Francis Marchlinski, Eugene Kholmovski, Nathan Burgon, Nan Hu, Lluis Mont, et al. Association of atrial tissue fibrosis identified by

delayed enhancement MRI and atrial fibrillation catheter ablation: the decaaf study. *JAMA*, 311(5):498–506, 2014.

[44] Robert S Oakes, Troy J Badger, Eugene G Kholmovski, Nazem Akoum, Nathan S Burgon, Eric N Fish, Joshua JE Blauer, Swati N Rao, Edward VR DiBella, Nathan M Segerson, et al. Detection and quantification of left atrial structural remodeling with delayed-enhancement magnetic resonance imaging in patients with atrial fibrillation. *Circulation*, 119(13):1758–1767, 2009.

[45] Demosthenes Katritsis, Mark A Wood, Eleftherios Giazitzoglou, Richard K Shepard, Georgia Kourlaba, and Kenneth A Ellenbogen. Long-term follow-up after radiofrequency catheter ablation for atrial fibrillation. *Europace*, 10(4):419–424, 2008.

[46] Li-Wei Lo, Yenn-Jiang Lin, Hsuan-Ming Tsao, Shih-Lin Chang, Ameya R Udyavar, Yu-Feng Hu, Kwo-Chang Ueng, Wen-Chin Tsai, Ta-Chun Tuan, Chien-Jung Chang, et al. The impact of left atrial size on long-term outcome of catheter ablation of chronic atrial fibrillation. *Journal of cardiovascular electrophysiology*, 20(11):1211–1216, 2009.

[47] Irene Hof, Karuna Chilukuri, Armin Arbab-Zadeh, Daniel Scherr, Darshan Dalal, Saman Nazarian, Charles Henrikson, David Spragg, Ronald Berger, Joseph Marine, et al. Does left atrial volume and pulmonary venous anatomy predict the outcome of catheter ablation of atrial fibrillation? *Journal of cardiovascular electrophysiology*, 20(9):1005–1010, 2009.

[48] Christian Sohns, Jan M Sohns, Dirk Vollmann, Lars Lüthje, Leonard Bergau, Marc Dorenkamp, Paul A Zwaka, Gerd Hasenfuß, Joachim Lotz, and Markus Zabel. Left atrial volumetry from routine diagnostic work up prior to pulmonary vein ablation is a good predictor of freedom from atrial fibrillation. *European Heart Journal–Cardiovascular Imaging*, 14(7):684–691, 2013.

[49] Roberto M Lang, Luigi P Badano, Victor Mor-Avi, Jonathan Afilalo, Anderson Armstrong, Laura Ernande, Frank A Flachskampf, Elyse Foster, Steven A Goldstein, Tatiana Kuznetsova, et al. Recommendations for cardiac chamber quantification by echocardiography in adults: an update from the american society of echocardiography and the european association of cardiovascular imaging. *European Heart Journal-Cardiovascular Imaging*, 16(3):233–271, 2015.

[50] Emelia J. Benjamin, Ralph B. D'Agostino, Albert J. Belanger, Philip A. Wolf, and Daniel Levy. Left atrial size and the risk of stroke and death. *Circulation*, 92(4):835–841, 1995.

[51] Marco R. Di Tullio, Ralph L. Sacco, Robert R. Sciacca, and Shunichi Homma. Left atrial size and the risk of ischemic stroke in an ethnically mixed population. *Stroke*, 30(10):2019–2024, 1999.

[52] Teresa SM Tsang, Marion E Barnes, Bernard J Gersh, Yasuhiko Takemoto, A Gabriela Rosales, Kent R Bailey, and James B Seward. Prediction of risk for first age-related cardiovascular events in an elderly population: the incremental value of echocardiography. *Journal of the American College of Cardiology*, 42(7):1199–1205, 2003.

[53] Teresa SM Tsang, Bernard J Gersh, Christopher P Appleton, A Jamil Tajik, Marion E Barnes, Kent R Bailey, Jae K Oh, Cynthia Leibson, Samantha C Montgomery, and James B Seward. Left ventricular diastolic dysfunction as a predictor of the first diagnosed nonvalvular atrial fibrillation in 840 elderly men and women. *Journal of the American College of Cardiology*, 40(9):1636–1644, 2002.

[54] Erlend Aune, Morten Baekkevar, Jo Roislien, Olaf Rodevand, and Jan Erik Otterstad. Normal reference ranges for left and right atrial volume indexes and ejection fractions obtained with real-time three-dimensional echocardiography. *European Journal of Echocardiography*, 10(6):738–744, 2009.

[55] Stanley Nattel and Masahide Harada. Atrial remodeling and atrial fibrillation: recent advances and translational perspectives. *Journal of the American College of Cardiology*, 63(22):2335–2345, 2014.

[56] GK Moe and JA Abildskov. Atrial fibrillation as a self-sustaining arrhythmia independent of focal discharge. *American heart journal*, 58(1):59–70, 1959.

[57] Sanjiv M Narayan, David E Krummen, Kalyanam Shivkumar, Paul Clopton, Wouter-Jan Rappel, and John M Miller. Treatment of atrial fibrillation by the ablation of localized sources: Confirm (conventional ablation for atrial fibrillation with or without focal impulse and rotor modulation) trial. *Journal of the American College of Cardiology*, 60(7):628–636, 2012.

[58] María S Guillem, Andreu M Climent, Miguel Rodrigo, Francisco Fernández-Avilés, Felipe Atienza, and Omer Berenfeld. Presence and stability of rotors in atrial fibrillation: evidence and therapeutic implications. *Cardiovascular research*, 109(4):480–492, 2016.

[59] João Salinet, Fernando S Schlindwein, Peter Stafford, Tiago P Almeida, Xin Li, Frederique J Vanheusden, María S Guillem, and G André Ng. Propagation of meandering rotors surrounded by areas of high dominant frequency in persistent atrial fibrillation. *Heart rhythm*, 14(9):1269–1278, 2017.

[60] Maurits Allessie and Natasja de Groot. Rotors during af: drivers or bystanders?, 2013.

[61] Geoffrey Lee, Saurabh Kumar, Andrew Teh, Andrew Madry, Steven Spence, Marco Larobina, John Goldblatt, Robin Brown, Victoria Atkinson, Simon Moten, et al. Epicardial wave mapping in human long-lasting persistent atrial fibrillation: transient rotational circuits, complex wavefronts, and disorganized activity. *European heart journal*, 35(2):86–97, 2013.

[62] Prashanthan Sanders, Omer Berenfeld, Mélèze Hocini, Pierre Jaïs, Ravi Vaidyanathan, Li-Fern Hsu, Stéphane Garrigue, Yoshihide Takahashi, Martin Rotter, Fréderic Sacher, et al. Spectral analysis identifies sites of high-frequency activity maintaining atrial fibrillation in humans. *Circulation*, 112(6):789–797, 2005.

[63] Ying-Chieh Liao, Jo-Nan Liao, Li-Wei Lo, Yenn-Jiang Lin, SHIH-Lin Chang, Yu-Feng Hu, Tze-Fan Chao, Fa-Po Chung, Ta-Chuan Tuan, Abigail Louise D Te, et al. Left atrial size and left ventricular end-systolic dimension predict the progression of paroxysmal atrial fibrillation after catheter ablation. *Journal of cardiovascular electrophysiology*, 28(1):23–30, 2017.

[64] Shih-Huang Lee, Ching-Tai Tai, Ming-Hsiung Hsieh, Chin-Feng Tsai, Yung-Kuo Lin, Hsuan-Ming Tsao, Wen-Chung Yu, Jin-Long Huang, Kow-Chang Ueng, Jun-Jack Cheng, et al. Predictors of early and late recurrence of atrial fibrillation after catheter ablation of paroxysmal atrial fibrillation. *Journal of Interventional Cardiac Electrophysiology*, 10(3):221–226, 2004.

[65] João Abecasis, Raquel Dourado, António Ferreira, Carla Saraiva, Diogo Cavaco, Katya Reis Santos, Francisco Belo Morgado, Pedro Adragão, and Aniceto Silva. Left atrial volume calculated by multi-detector computed tomography may predict successful pulmonary vein isolation in catheter ablation of atrial fibrillation. *Europace*, 11(10):1289–1294, 2009.

[66] Dominic Y Leung, Anita Boyd, Arnold A Ng, Cecilia Chi, and Liza Thomas. Echocardiographic evaluation of left atrial size and function: current understanding, pathophysiologic correlates, and prognostic implications. *American heart journal*, 156(6):1056–1064, 2008.

[67] Teresa SM Tsang, Walter P Abhayaratna, Marion E Barnes, Yoko Miyasaka, Bernard J Gersh, Kent R Bailey, Stephen S Cha, and James B Seward. Prediction of cardiovascular outcomes with left atrial size: is vol-

ume superior to area or diameter? *Journal of the American College of Cardiology*, 47(5):1018–1023, 2006.

[68] Jacob S Koruth, E Kevin Heist, Stephan Danik, Conor D Barrett, Rajesh Kabra, Dan Blendea, Jeremy Ruskin, and Moussa Mansour. Accuracy of left atrial anatomical maps acquired with a multielectrode catheter during catheter ablation for atrial fibrillation. *Journal of interventional cardiac electrophysiology*, 32(1):45, 2011.

[69] Roberto Rordorf, Enrico Chieffo, Simone Savastano, Alessandro Vicentini, Barbara Petracci, Valentina De Regibus, Adele Valentini, Catherine Klersy, Roberto Dore, and Maurizio Landolina. Anatomical mapping for atrial fibrillation ablation: A head-to-head comparison of ultrasound-assisted reconstruction versus fast anatomical mapping. *Pacing and Clinical Electrophysiology*, 38(2):187–195, 2015.

[70] Yasuo Okumura, Ichiro Watanabe, Masayoshi Kofune, Koichi Nagashima, Kazumasa Sonoda, Hiroaki Mano, Kimie Ohkubo, Toshiko Nakai, Naoko Sasaki, Rikitake Kogawa, et al. Effect of catheter tip-tissue surface contact on three-dimensional left atrial and pulmonary vein geometries: Potential anatomic distortion of 3d ultrasound, fast anatomical mapping, and merged 3d ct-derived images. *Journal of cardiovascular electrophysiology*, 24(3):259–266, 2013.

[71] Frederick T Han and Nassir Marrouche. An atrial fibrosis-based approach for atrial fibrillation ablation. *Future cardiology*, 11(6):673–681, 2015.

[72] James A Sethian. Curvature and the evolution of fronts. *Communications in Mathematical Physics*, 101(4):487–499, 1985.

[73] Michael Felsberg and Gerald Sommer. The monogenic signal. *IEEE Transactions on Signal Processing*, 49(12):3136–3144, 2001.

[74] Mark G Rabbat, David Wilber, Kevin Thomas, Owais Malick, Atif Bashir, Anoop Agrawal, Santanu Biswas, Thriveni Sanagala, and Mushabbar A

Syed. Left atrial volume assessment in atrial fibrillation using multimodality imaging: a comparison of echocardiography, invasive three-dimensional carto and cardiac magnetic resonance imaging. *The international journal of cardiovascular imaging*, 31(5):1011–1018, 2015.

[75] Jadranka Stojanovska, Paul Cronin, Barry H Gross, Ella A Kazerooni, Alex Tsodikov, Luba Frank, and Hakan Oral. Left atrial function and maximum volume as determined by mdct are independently associated with atrial fibrillation. *Academic radiology*, 21(9):1162–1171, 2014.

[76] Qian Tao, Esra Gucuk Ipek, Rahil Shahzad, Floris F Berendsen, Saman Nazarian, and Rob J van der Geest. Fully automatic segmentation of left atrium and pulmonary veins in late gadolinium-enhanced MRI: Towards objective atrial scar assessment. *Journal of Magnetic Resonance Imaging*, 44(2):346–354, 2016.

[77] Chao Ma, Gongning Luo, and Kuanquan Wang. A combined random forests and active contour model approach for fully automatic segmentation of the left atrium in volumetric MRI. *BioMed research international*, 2017, 2017.

[78] Barbara Kircher, Joseph A Abbott, Stanley Pau, Robert G Gould, Ronald B Himelman, Charles B Higgins, Martin J Lipton, and Nelson B Schiller. Left atrial volume determination by biplane two-dimensional echocardiography: validation by cine computed tomography. *American heart journal*, 121(3):864–871, 1991.

[79] Hye Mi Gweon, Sang Jin Kim, Tae Hoon Kim, Sang Min Lee, Yoo Jin Hong, and Se-Joong Rim. Evaluation of left atrial volumes using multidetector computed tomography: comparison with echocardiography. *Korean journal of radiology*, 11(3):286–294, 2010.

[80] Nazem Akoum, Marcos Daccarett, Chris McGann, Nathan Segerson, Gaston Vergara, Suman Kuppahally, Troy Badger, Nathan Burgon, Thomas Haslam, Eugene Kholmovski, et al. Atrial fibrosis helps select the ap-

propriate patient and strategy in catheter ablation of atrial fibrillation: A DE-MRI guided approach. *Journal of cardiovascular electrophysiology*, 22(1):16–22, 2011.

[81] Procolo Marchese, Vincenzo Malavasi, Luca Rossi, Natalia Nikolskaya, Grazia Delle Donne, Mirza Becirovic, Alessandra Colantoni, Antonio Luciani, and Maria Grazia Modena. Indexed left atrial volume is superior to left atrial diameter in predicting nonvalvular atrial fibrillation recurrence after successful cardioversion: a prospective study. *Echocardiography*, 29(3):276–284, 2012.

[82] Christian Mahnkopf, Troy J Badger, Nathan S Burgon, Marcos Daccarett, Thomas S Haslam, Christopher T Badger, Christopher J McGann, Nazem Akoum, Eugene Kholmovski, Rob S Macleod, et al. Evaluation of the left atrial substrate in patients with lone atrial fibrillation using delayed-enhanced MRI: implications for disease progression and response to catheter ablation. *Heart Rhythm*, 7(10):1475–1481, 2010.

[83] Josien PW Pluim, JB Antoine Maintz, and Max A Viergever. Mutual-information-based registration of medical images: a survey. *IEEE transactions on medical imaging*, 22(8):986–1004, 2003.

[84] Roger P Woods, Simon R Cherry, and John C Mazziotta. Rapid automated algorithm for aligning and reslicing PET images. *Journal of computer assisted tomography*, 16(4):620–633, 1992.

[85] Roger P Woods, John C Mazziotta, Simon R Cherry, et al. MRI-PET registration with automated algorithm. *Journal of computer assisted tomography*, 17(4):536–546, 1993.

[86] Jane Dewire, Irfan M Khurram, Farhad Pashakhanloo, David Spragg, Joseph E Marine, Ronald D Berger, Hiroshi Ashikaga, John Rickard, Stefan L Zimmerman, Vadim Zipunnikov, et al. The association of pre-existing left atrial fibrosis with clinical variables in patients referred for

catheter ablation of atrial fibrillation. *Clinical Medicine Insights. Cardiology*, 8(Suppl 1):25, 2014.

[87] Yingli Lu, Yuesong Yang, Kim A Connelly, Graham A Wright, and Perry E Radau. Automated quantification of myocardial infarction using graph cuts on contrast delayed enhanced magnetic resonance images. *Quantitative imaging in medicine and surgery*, 2(2):81, 2012.

[88] Thomas A Dewland, Max Wintermark, Anna Vaysman, Lisa M Smith, Elizabeth Tong, Eric Vittinghoff, and Gregory M Marcus. Use of computed tomography to identify atrial fibrillation associated differences in left atrial wall thickness and density. *Pacing and Clinical Electrophysiology*, 36(1):55–62, 2013.

[89] Jiro Inoue, John SH Baxter, and Maria Drangova. Left atrial wall segmentation from ct for radiofrequency catheter ablation planning. In *Workshop on Clinical Image-Based Procedures*, pages 71–78. Springer, 2015.

[90] Jiro Inoue, Allan C Skanes, James A White, Martin Rajchl, and Maria Drangova. Patient-specific left atrial wall-thickness measurement and visualization for radiofrequency ablation. *SPIE Medical Imaging, Proceedings of SPIE Medical Imaging*, 9036:90361N–90361N, 2014.

[91] Shuman Jia, Loïc Cadour, Hubert Cochet, and Maxime Sermesant. Stacom-slawt challenge: left atrial wall segmentation and thickness measurement using region growing and marker-controlled geodesic active contour. In *International Workshop on Statistical Atlases and Computational Models of the Heart*, pages 211–219. Springer, 2016.

[92] Pawel Kuklik, Stef Zeemering, Bart Maesen, Jos Maessen, Harry J Crijns, Sander Verheule, Anand N Ganesan, and Ulrich Schotten. Reconstruction of instantaneous phase of unipolar atrial contact electrogram using a concept of sinusoidal recomposition and hilbert transform. *IEEE transactions on biomedical engineering*, 62(1):296–302, 2015.

[93] Tobias Oesterlein, Daniel Frisch, Axel Loewe, Gunnar Seemann, Claus Schmitt, Olaf Dössel, and Armin Luik. Basket-type catheters: Diagnostic pitfalls caused by deformation and limited coverage. *BioMed research international*, 2016, 2016.

[94] S Zeemering, B Maesen, J Nijs, DH Lau, M Granier, S Verheule, and U Schotten. Automated quantification of atrial fibrillation complexity by probabilistic electrogram analysis and fibrillation wave reconstruction. In *Engineering in Medicine and Biology Society (EMBC), 2012 Annual International Conference of the IEEE*, pages 6357–6360. IEEE, 2012.

[95] Jason Ng, Alan H Kadish, and Jeffrey J Goldberger. Technical considerations for dominant frequency analysis. *Journal of cardiovascular electrophysiology*, 18(7):757–764, 2007.

[96] L Martinez-Mateu, L Romero, A Ferrer-Albero, R Sebastian, Matas JF Rodríguez, J Jalife, O Berenfeld, and J Saiz. Factors affecting basket catheter detection of real and phantom rotors in the atria: A computational study. *PLoS computational biology*, 14(3):e1006017, 2018.

[97] Omid Sayadi, Mohammad B Shamsollahi, and Gari D Clifford. Synthetic ecg generation and bayesian filtering using a gaussian wave-based dynamical model. *Physiological measurement*, 31(10):1309, 2010.

[98] Patrick E McSharry, Gari D Clifford, Lionel Tarassenko, and Leonard A Smith. A dynamical model for generating synthetic electrocardiogram signals. *IEEE transactions on biomedical engineering*, 50(3):289–294, 2003.

[99] Sailes K Sengijpta. Fundamentals of statistical signal processing: Estimation theory, 1995.

[100] MW Rivolta, LT Mainardi, R Sassi, and VDA Corino. Synthetic atrial electrogram generator. In *XIII Mediterranean Conference on Medical and Biological Engineering and Computing 2013*, pages 670–673. Springer, 2014.

[101] Valentina DA Corino, Frida Sandberg, Luca T Mainardi, and Leif Sornmo. An atrioventricular node model for analysis of the ventricular response during atrial fibrillation. *IEEE Transactions on Biomedical Engineering*, 58(12):3386–3395, 2011.

[102] B Stender, B Wang, and A Schlaefer. Computing synthetic echocardiography volumes for automatic validation of 3d segmentation results. *Biomedical Engineering/Biomedizinische Technik*, 57(SI-1 Track-B):123–127, 2012.

[103] Paul Gammans, SF Qin, and DK Wright. The synthesis of emg signals based on considerations of signal spectra. *Biomedical sciences instrumentation*, 39:187–192, 2003.

[104] Pawel Kuklik, Stef Zeemering, Arne van Hunnik, Bart Maesen, Laurent Pison, Dennis H Lau, Jos Maessen, Piotr Podziemski, Christian Meyer, Benjamin Schäffer, et al. Identification of rotors during human atrial fibrillation using contact mapping and phase singularity detection: technical considerations. *IEEE Transactions on Biomedical Engineering*, 64(2):310–318, 2017.

[105] G Seemann, FB Sachse, M Karl, DL Weiss, V Heuveline, and O Dössel. Framework for modular, flexible and efficient solving the cardiac bidomain equations using PETSc. In *Progress in industrial mathematics at ECMI 2008*, pages 363–369. Springer, 2010.

[106] Axel Loewe, Martin W Krueger, Fredrik Holmqvist, Olaf Dössel, Gunnar Seemann, and Pyotr G Platonov. Influence of the earliest right atrial activation site and its proximity to interatrial connections on p-wave morphology. *EP Europace*, 18(suppl_4):iv35–iv43, 2016.

[107] Axel Loewe, Mathias Wilhelms, Fathima Fischer, Eberhard P Scholz, Olaf Dössel, and Gunnar Seemann. Arrhythmic potency of human ether-a-go-go-related gene mutations l532p and n588k in a computational model of human atrial myocytes. *Europace*, 16(3):435–443, 2014.